Ocean Engineering 311 (2024) 118732

Contents lists available at ScienceDirect

Ocean Engineering

journal homepage: www.elsevier.com/locate/oceaneng

Research paper

Modelling the acoustic radiation of propeller tip vortex cavitation in potential flow simulations

Joseph Praful Tomy [a,b,*], Roland Gosda [c], Stephan Berger [b,d], Harry B. Bingham [a], Poul Andersen [a], Moustafa Abdel-Maksoud [c]

[a] Technical University of Denmark, Department of Civil and Mechanical Engineering, Kgs. Lyngby, Denmark
[b] MAN Energy Solutions, Propeller & Aft Ship Department, Denmark
[c] Technical University of Hamburg, Institute for Fluid Dynamics and Ship Theory, Hamburg, Germany
[d] FORCE Technology, Hydro- and Aerodynamics Department, Kgs. Lyngby, Denmark

ARTICLE INFO

Keywords:
Partial cavitation
Tip-vortex cavitation
Acoustic
Panel method
Cavitation
Underwater radiated noise
Ffowcs-Williams Hawkings

ABSTRACT

Propeller cavitation and its effect on underwater radiated noise (URN) are topics of increasing interest within the marine hydrodynamics community. Numerical prediction of the URN characteristics of a given propeller design is vital in achieving the design of low-noise propellers. In this context, the current paper investigates different acoustic models for the numerical evaluation of propeller tip vortex cavitation-induced-noise, using potential flow simulations. Two acoustic modelling approaches are discussed, considering an elongated cylindrical representation of helical tip vortex cavities. Model 2D is a two-dimensional geometrical representation of the tip vortex cavity, wherein equivalent acoustic sources are defined along the cavity surface. Model 1D is an axisymmetric one-dimensional model with equivalent point sources that are distributed along the cavity axis. The applicability and limitations of the two acoustic models are assessed through a verification study of an analytical case for harmonic oscillations of a circular cylinder. The influence and sensitivity of important parameters are discussed, along with their relevance and application when extended to typical tip vortex cavity structures emanating from ship propellers. Finally, the practicality of the acoustic models for propeller tip vortex cavities is investigated through a validation study for the 'Princess Royal' propeller. The hydrodynamic flow solution is obtained from a potential flow solver, which includes flow models for sheet cavitation and tip vortex cavitation. Tip vortex cavity acoustics is obtained using the time-varying tip vortex cavity geometry from the potential flow solution. Acoustic contributions due to the blade rotation and sheet cavity fluctuations are separately computed. The simulation results are then compared with experimental measurements.

1. Introduction

Underwater acoustics is the study of the occurrence and propagation of sound in water, and how it affects the performance of other entities present in the ocean environment. This includes many vital processes such as orientation and communication between aquatic animals. From a technical point of view, accurate modelling of sound propagation plays an important role in various processes such as: identification of aquatic species by hydrographic research vessels (De Robertis and Handegard, 2012), stealth operation of naval vessels (Moore, 2019), and ocean data collection using hydrophone sensors and echo-sounders (Mitson and Knudsen, 2003). The common feature of all these operational scenarios is that the extent of background ocean noise is critical to ensure smooth operation. All these operations are primarily based on the principle of hydro-acoustic wave propagation or what is commonly referred to as underwater sound.

An interesting and often posed question in this context is: what is the difference between sound, signal, and noise? The ocean environment contains a large variety of acoustic pressure waves, generated from different sources. Sound is a general term for acoustic pressure fluctuations that are propagated through the medium, inducing changes in its density (Ainslie et al., 2021). Which among these can be classified as signal, and which can be classified as noise? The answer is more psychological than physical. For any of the operational scenarios mentioned earlier, if the acoustic waves present in the environment interfere with the smooth operation of the system, then these are classified as noise (Ross, 1976). Acoustic waves that are desirable for the

* Corresponding author at: MAN Energy Solutions, Propeller & Aft Ship Department, Denmark.
E-mail addresses: joseph.tomy@man-es.com (J.P. Tomy), roland.gosda@tuhh.de (R. Gosda), ssb@forcetechnology.com (S. Berger), hbbi@dtu.dk (H.B. Bingham), poula@dtu.dk (P. Andersen), m.abdel-maksoud@tuhh.de (M. Abdel-Maksoud).

https://doi.org/10.1016/j.oceaneng.2024.118732
Received 6 February 2024; Received in revised form 8 July 2024; Accepted 13 July 2024
Available online 9 August 2024

Nomenclature

Abbreviations

BEM	Boundary Element Method
BPF	Blade Passing Frequency
CFD	Computational Fluid Dynamics
DTU	Technical University of Denmark
FWH	Ffowcs-Williams–Hawkings
ISO	International Organization for Standardization
ITTC	International Towing Tank Conference
LMIP	Lloyd-Mirror Interference Pattern
PSD	Power Spectral Density
RPM	Revolutions Per Minute
SBF	Solid Boundary Factor
SL	Source Level
SPL	Sound Pressure Level
TUHH	Technical University of Hamburg
TVC	Tip Vortex Cavity (or Cavitation)
URN	Underwater Radiated Noise

Greek symbols

α	Wave number of the surface wave
Δf_{smear}	Frequency band, in Hz, over which noise spectrum around the tonals are smeared out
$\Delta\psi$	$= 0.5°$, Rotation of the propeller per time step.
Γ	Circulation of a cavitating tip vortex segment
Γ_b	Maximum bound circulation
Γ_{ini}	Initial circulation
γ_{ini}	Fraction of maximum bound circulation that is assumed for calculating initial circulation
λ_x	Wavelength of surface wave
ρ	Fluid density
ρ_0	Fluid density in the undisturbed medium
σ	Eigenfrequency of surface wave
σ_n	$= \frac{p_0 - p_v + \rho g z_{\text{hub}}}{1/2 \rho n^2 D^2}$, Cavitation number
θ	Co-ordinate along the tangential direction of the cavity surface
Υ	Fluctuating cavity radius
Υ_{eqm}	Equilibrium cavity radius
$\bar{\Upsilon}$	Mean cavity radius
Υ_D	Domain radius used in the integration of the two-dimensional Rayleigh–Plesset equation
$\tilde{\Upsilon}$	Amplitude of cavity radius fluctuations
ξ	Co-ordinate along the radial direction of the cavity surface

Latin symbols

c	Speed of sound
c_x	Speed of propagation of surface wave
dS	Surface area of an element on surface S
dx	Length along the axial direction of discrete cavity surface element
f	Frequency of the sound waves
g	Acceleration due to gravity
h	Integer corresponding to the degree of blade harmonic
h_{cav}	Span-wise average of the sheet cavity thickness at the blade trailing edge
i	Index for elements along the cavity circumferential direction
j	Index for elements along the cavity axial direction
k	Acoustic wave number
$L_{1\text{rev}}$	Helical wavelength, i.e. helical length traversed by the cavity surface wave during one propeller revolution
L_x	Axial length of cavity
n	Number of propeller revolutions per second
n_{Mode}	Tip vortex cavity mode shape
n_θ	Number of elements in the circumferential direction, for Model 2D
n_{ax}	Number of elements along the axial direction
n_t	Number of time steps, per surface wave period
n_x	Number of elements in the axial direction, per surface wavelength
p_c	Pressure inside the cavity
p_D	Ambient pressure far away from the vortex axis, at $\xi = \Upsilon_D$
p_{g0}	Initial gas pressure inside cavity
p_L	Loading induced noise component
p_{ref}	Acoustic pressure amplitude from analytical solution in Eq. (9)
p_{sim}	Acoustic wave amplitude from the numerical simulation
p_T	Thickness induced noise component
p_v	Vapour pressure of water
p_{vtx}	Pressure due to vortex
$\tilde{p}$	Acoustic pressure
r	Radial coordinate of observer point
R^2	Coefficient of determination in regression analysis
r_0	$= \|\|\boldsymbol{r}\|\|$, Scalar distance from $\boldsymbol{x}$ to $\boldsymbol{y}$
$\breve{R}_{\text{btm}}$	Reflection coefficient at the sea bottom
r_{sph}	Radius of equivalent sphere in Model 1D
r_{sr}	Range between the source and receiver
r_{vc}	Viscous core radius of the tip vortex cavity
T_p	$= 1/n$, Time period for one propeller revolution
u_θ	Circumferential flow velocity around the vortex core
x	Co-ordinate along the axial direction of the cavity surface
z_{hub}	Depth of propeller hub centre
z_r	Depth of receiver
z_s	Depth of source

Operators/Functions

$\delta(f_s)$	Dirac-delta function
∇	Spatial gradient operator
∂	Partial differential operator
$\Box$	$= \frac{1}{c^2}\frac{\partial^2}{\partial t^2} - \nabla^2$, d'Alembertian operator or wave operator
$f_s = 0$	Function that describes the acoustic source surface
$H(f_s)$	Heaviside function

H_0'	First derivative of the Hankel function of the first kind, of order zero
H_0	Hankel function of the first kind, of order zero
$_{ret}$	Function evaluated at retarded time

Vector/Tensor quantities

$\boldsymbol{l}$	$= \tilde{p}\hat{\boldsymbol{n}}$, Local force intensity vector due to surface pressure $\tilde{p}$
l_i	$= \tilde{p}\hat{n}_i$, Local force intensity vector due to surface pressure $\tilde{p}$
$\boldsymbol{M}$	$= \boldsymbol{v}/c$, Mach number vector
$\hat{\boldsymbol{n}}$	Unit normal vector
$\boldsymbol{r}$	$= \boldsymbol{y} - \boldsymbol{x}$, Radiation vector from the source at $\boldsymbol{x}$ to the observer at $\boldsymbol{y}$
$\hat{\boldsymbol{r}}$	$= \frac{\boldsymbol{r}}{r_0}$, Unit vector in the radiation direction
T_{ij}	Lighthill stress tensor
$\boldsymbol{U}$	$= \boldsymbol{v} + \frac{\rho}{\rho_0}(\boldsymbol{u} - \boldsymbol{v})$
$\boldsymbol{u}$	Fluid velocity
$\boldsymbol{v}$	Surface moving velocity
$\boldsymbol{v}_{\text{def}}$	Velocity due to cavity surface deformation
$\boldsymbol{x}$	Position vector of acoustic source
$\boldsymbol{y}$	Position vector of observer

operations, can generally be classified as signals. For example, acoustic waves generated by an echosounder are 'signals' to the measurement sensor, but 'noise' to a whale that is trying to communicate to its companions.

Under the premise that underwater noise is prevalent in all ocean acoustic operational environments, it is important to have simulation methods to predict the origin and propagation of undesirable noise. An important noise source in most ocean environments is the noise radiated by ship propellers. In all the examples of oceanic operations mentioned above, the acoustic waves generated by the propeller can be categorized as undesirable noise. Moreover, the intensity of this noise source is high, such that it is propagated over large distances in the ocean.

Propeller noise is characterized by narrowband spectral peaks at multiples of the blade passing frequency (BPF), along with a broadband spectrum that is predominant at higher frequencies. A typical example of a propeller noise spectrum is shown in Fig. 1. The distinct peaks at lower frequencies are at multiples of the blade passing frequency, also known as tonal noise. Large scale cavity dynamics, such as the growth and shrinkage of fully developed cavities, contribute to the tonal noise as well as the low- to medium-frequency broadband noise. The tonal noise contribution is from the dependence of the cavity volume on the blade position in a ship wake field; whereas the broadband noise contribution can be attributed to stochastic variations of the cavity volume due to turbulent inflow. The broadband spectrum at higher frequencies is attributed to rapid, volatile processes occurring in the flow field, such as flow turbulence, eddies and small-scale cavity structures.

The unpredictable nature of the high-frequency processes makes it difficult to deterministically compute and predict their acoustic characteristics. This is the reason why stochastic and empirical models are frequently employed in the determination of the high frequency, broadband spectrum (Bosschers, 2018a). On the other hand, unlike the broadband component, the narrowband peaks can be obtained deterministically based on the propeller operating conditions. Moreover, a large portion of the acoustic energy in the propeller noise spectrum is attributed to the tonal noise. However, the deterministic evaluation of the tonal noise is not a trivial task, considering the number of interlinked physical principles that contribute to these sharp peaks. The

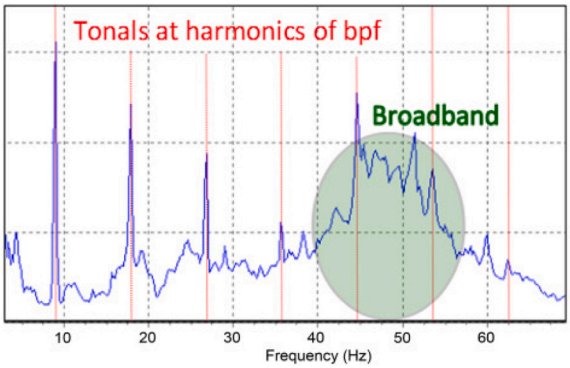

Fig. 1. Example of a pressure amplitude spectrum of a propeller, with predominant tip-vortex cavitation. Pressure amplitudes on the vertical axis are on a linear scale. *Source:* Reproduced from van Wijngaarden et al. (2005).

propeller blade rotation causes a fluctuating fluid volume displacement, which is then radiated as blade thickness induced noise. Blade loading induced noise occurs due to the unsteady loading on the propeller blades, which is dramatically augmented by a non-uniform ship wake field. The formation of sheet cavity surfaces on the blade is directly linked to the pressure distribution on the blade surface, and hence, also follows a periodic behaviour. In many cases, the gradient of blade bounded circulation reaches a maximum value at the blade tip, which contributes to the formation of a tip vortex cavity with a fluctuating shape. All these phenomena are interlinked and consequently, the acoustic noise generated from all of them occurs predominantly at multiples of the blade passing frequency. An accurate deterministic model for propeller acoustics should include the effects of all these phenomena.

Finite-volume-based numerical solvers have been employed extensively over the past few years to simulate deterministic propeller problems (Sezen and Atlar, 2022). However, the requirements for a large computational domain, and small element sizes in order to capture the acoustic waves, make them impractical for underwater acoustic problems. In addition, one of the major drawbacks of finite-volume-based numerical solvers for acoustic evaluation is that the contribution from the various acoustic sources cannot be separated. This is especially important in propeller noise mitigation strategies, where an understanding of the relative contribution of the interlinked noise mechanisms can have a profound impact. For example, a fully-resolved Navier–Stokes equation solver can provide a reasonably accurate prediction of the overall acoustic noise due to propeller rotation; but, the distinction between acoustic radiation due to sheet cavity and tip vortex cavity fluctuations is difficult to make.

This overview highlights the requirement of robust numerical models which can be employed to independently assess the acoustic contribution from cavities due to the propeller flow. Boundary Element Method (BEM) based models for the evaluation of sheet cavity-induced-noise have been previously proposed (Testa, 2008; Göttsche, 2020). This paper aims to provide a comprehensive investigation of a similar approach for tip vortex cavity-induced-noise. The acoustic formulations are initially verified with analytical solutions, and thereafter validated with a propeller case study, thereby providing an in-depth analysis of the merits and limitations of the approach.

2. Background and contributions of the current work

The mathematical framework for underwater hydroacoustics is based on equivalent theoretical formulations in aeroacoustics. In the 1940s, with the rapid advancement of the aircraft industry, a lot of impetus was put on auxiliary research, such as noise radiated from aircraft. This led to the rise of some of the fundamental mathematical

formulations used in aeroacoustics, and by extension in hydroacoustics. However, one of the major points of difference is the effect of cavitation on the radiated noise of underwater propellers. The significant effect of cavitation on underwater noise led to a parallel branch of study, focusing on cavity dynamics and acoustics.

In this section, a literature study is conducted, which aims to serve as a platform for the formulation and implementation of the numerical acoustic models for tip vortex cavitation. Initially, the origin and validity regimes of the fundamental equations for acoustics of surfaces in motion are explored, under Section 2.1. Thereafter, in Section 2.2, a contemporary update about the numerical implementation of tip vortex cavitation acoustics is provided.

2.1. Numerical modelling of acoustics

The basis for numerical modelling of acoustics is the acoustic wave Eq. (1), which describes the propagation of sound waves in a homogeneous, inviscid fluid. It is derived from a combination of the conservation of mass and momentum equations with the adiabatic equation of state for a compressible fluid, for the fluctuating pressure component (i.e. the acoustic pressure, $\tilde{p}$).

$$\nabla^2\tilde{p} - \frac{1}{c^2}\frac{\partial^2\tilde{p}}{\partial t^2} = 0 \qquad \text{(1, Acoustic Wave Equation)}$$

In 1952, Lighthill published his theory of aeroacoustics (Lighthill, 1952), which describes the propagation of acoustic waves generated by turbulence in a fluid flow. This was the origin of the classical acoustic analogy, which treats the fluid flow and the acoustic sound propagation as two separate problems. According to the Lighthill equation, the turbulent fluid flow can be described by equivalent acoustic sources. Such sources can then be treated within an acoustic solver that does not need to account for any interactions with the fluid flow. The entire noise generation process is mathematically reduced to the study of wave propagation in a quiescent medium with the fluid flow replaced by acoustic sources.

The next significant advancement in the mathematical understanding of noise propagation was provided by Ffowcs-Williams and Hawkings in their 1969 paper (Ffowcs-Williams and Hawkings, 1969), wherein the Lighthill theory was extended to include the arbitrary convective motion of surfaces. This equation – the Ffowcs-Williams Hawkings (FWH) equation (2) – is now widely used as the governing equation for numerical implementations of noise propagating from rotating machinery. The use of the FWH equation allows the noise sources to be separated into three constituents — thickness induced, loading induced and quadrupole noise sources. These noise sources are representative of physical processes associated with the noise propagation phenomenon.

$$\Box\tilde{p} = \frac{\partial}{\partial t}[\rho_0\delta(f_s)U\cdot\hat{n}] - \frac{\partial}{\partial x_i}[l_i\delta(f_s)] + \frac{\partial^2}{\partial x_i\partial x_j}[T_{ij}H(f_s)] \qquad \text{(2, FWH Equation)}$$

The FWH equation is ideally suited for integration into Computational Fluid Dynamics (CFD) methods, in the evaluation of noise propagation due to surfaces in motion. The acoustic analogy avoids the requirement for a large computational domain. The non-linear problem of noise generation by a moving surface is effectively converted into a linear problem in the FWH equation. All the non-linear effects are assembled in the quadrupole term of the FWH equation. Using physical reasoning for certain flow applications, the entire FWH equation can essentially be converted into a linear problem, and closed form solutions can be obtained (Farassat and Brentner, 1998).

The most commonly implemented among such closed form solutions is the Farrassat 1A formulation (Farassat and Succi, 1982; Brentner and Farassat, 2003; Farassat, 2007), as seen in Eq. (3). This is a further simplification of the FWH equation for rotating blades, with a subsonic Mach number. The effect of the simplification is that only the linear part of the noise sources, i.e. the thickness induced and loading induced noise, are retained. The thickness induced noise represents the noise generated due to fluid displacement, while the loading induced noise describes the noise due to unsteady loading on the solid surface. The linearity of the simplified problem allows the discretization of the noise sources. In the case of the noise generated by a propeller blade, the blade surface can be discretized into small elements, and equivalent noise contributions can be obtained for each element. From the perspective of numerical implementation, this allows the employment of efficient numerical schemes that enable the numerical integration of the noise contributions at the source locations (i.e. the blade surface).

$$\tilde{p}(\boldsymbol{x},t) = p_T(\boldsymbol{x},t) + p_L(\boldsymbol{x},t) \tag{3a}$$

$$p_T(\boldsymbol{x},t) = \frac{\rho_0}{4\pi}\int_S\left[\frac{\dot{\boldsymbol{v}}\cdot\hat{\boldsymbol{n}} + \boldsymbol{v}\cdot\dot{\hat{\boldsymbol{n}}}}{r_0|1-\boldsymbol{M}\cdot\hat{\boldsymbol{r}}|^2}\right]_{\text{ret}}\mathrm{dS} + \frac{\rho_0}{4\pi}\int_S\left[\frac{\boldsymbol{v}\cdot\hat{\boldsymbol{n}}\left(r\dot{\boldsymbol{M}}\cdot\hat{\boldsymbol{r}} + c\boldsymbol{M}\cdot\hat{\boldsymbol{r}} - c\|\boldsymbol{M}\|^2\right)}{r_0^2|1-\boldsymbol{M}\cdot\hat{\boldsymbol{r}}|^3}\right]_{\text{ret}}\mathrm{dS} \tag{3b}$$

$$p_L(\boldsymbol{x},t) = \frac{1}{4\pi c}\int_S\left[\frac{\dot{\boldsymbol{l}}\cdot\hat{\boldsymbol{r}}}{r_0|1-\boldsymbol{M}\cdot\hat{\boldsymbol{r}}|^2}\right]_{\text{ret}}\mathrm{dS} + \frac{1}{4\pi}\int_S\left[\frac{\boldsymbol{l}\cdot\hat{\boldsymbol{r}} - \boldsymbol{l}\cdot\boldsymbol{M}}{r_0|1-\boldsymbol{M}\cdot\hat{\boldsymbol{r}}|^2}\right]_{\text{ret}}\mathrm{dS} + \frac{1}{4\pi c}\int_S\left[\frac{\boldsymbol{l}\cdot\hat{\boldsymbol{r}}\left(r\dot{\boldsymbol{M}}\cdot\hat{\boldsymbol{r}} + c\boldsymbol{M}\cdot\hat{\boldsymbol{r}} - c\|\boldsymbol{M}\|^2\right)}{r_0^2|1-\boldsymbol{M}\cdot\hat{\boldsymbol{r}}|^3}\right]_{\text{ret}}\mathrm{dS}, \tag{3c}$$

2.2. Acoustics of tip vortex cavities

When a propeller rotates in the wake field of the ship, vortices are formed at the blade tip due to the pressure difference between the suction and pressure sides. Such a region of swirling fluid motion, which is then swept downstream in a helical pattern, is often referred to as a tip vortex. The helical cavity formed by the region of reduced pressure is termed the tip vortex cavity. The inflow velocity and the thrust loading on the propeller excite fluctuations in shape and size of the tip vortex cavity. These fluctuations of the tip vortex cavity radiate acoustic pressure waves into the flow environment, which are perceived as the acoustic contribution of the tip vortex.

The regularity in the shape of vortices and its resemblance to an elongated cylinder has led to considerable research focused on the development of analytical solutions of such vortex cavities. The vibrations of the columnar vortex were first investigated by Thomson, as early as 1880. Thomson (1880) provides a mathematical description of the incompressible fluid flow due to axi-symmetric vibrations around the vortex axis. Ffowcs-Williams and O'shea (1970) extended the analysis for compressible flow, where the cavity surface interface is excited by the pressure field. The analysis was broadened by Morozov (1974) for harmonic oscillations. Morozov provides a generic solution for the radiated sound field due to harmonic oscillations of an infinite cylinder.

An important aspect of the analytical solutions pertains to their extent of validity in a computational domain. The assumptions used in the derivation of the analytical solutions lead to their validity extents. For example, both the solutions proposed by Ffowcs-Williams and O'shea (1970) and Morozov (1974) are valid only for small amplitude oscillations. Similar restrictions are also applicable to the wavelength of the surface propagating wave, and the distance of the receiver point. These limitations restrict the applicability of the mathematical models to the case of a realistic propeller tip vortex cavity. Nevertheless, their accuracy within the applicable extents of validity serves as a valuable tool for verifying numerical implementations.

A caveat of the mathematical formulations is that they are only valid for the familiar modes of cavity fluctuations. Many of the analytical solutions are based on linear wave theory; whereas in reality, the interaction between the sheet cavities formed around the blade surface

and the tip vortices may result in highly non-linear phenomena such as cavity splitting and coalescence (Choi and Chahine, 2003; Gosda et al., 2021). Assessing the influence of such phenomena on the low-frequency broadband noise spectra is a formidable task, and a practical approach is to rely on semi-empirical models such as the one proposed in Bosschers (2018b). Strong interactions between cavity fluctuations and flow instability may also result in a discrete tonal noise of high amplitude, which is referred to as vortex singing. It was first reported by Higuchi et al. (1989-12), and later investigated by Maines and Arndt (1997) and Arndt et al. (2015). The irregularity of the tip vortex cavity shape caused by the sheet cavity interaction is one of the major challenges encountered when applying the analytical and computational models.

From the perspective of numerical hydroacoustics, the analytical solutions from geometrical approximations may not always produce the desired results, especially for complex and dynamic geometries such as the cavity surfaces due to propeller flow. Hence, industrial applications prefer numerical simulations based on computational fluid dynamics. Surface integral formulations are often employed in such applications because they are computationally cheaper when compared to finite-volume solutions. Seybert et al. (1986) present a surface integral formulation for acoustic scattering and radiation for harmonic excitation of axisymmetric bodies based on the Helmholtz equation. Ligneul (1988) proposed a theoretical formulation based on Green's functions for interfaces similar to propeller tip vortex cavities, by deriving the cavity interface perturbations from a Rayleigh–Plesset-type equation. A commonly adopted surface integral formulation in hydroacoustics is the Farrassat −1A formulation of the Ffowcs-William–Hawkings equation Eq. (3). In such acoustic analogy approaches, data surfaces (permeable or impermeable) are defined such that they enclose the major propeller acoustic source mechanisms. The propeller acoustic behaviour is then estimated through surface integrals over the data surface, replacing cumbersome volume integral formulations (ITTC, 2017).

2.3. Aim of the current paper

The aim of the current paper is to investigate two different discretization approaches that can be employed in the computational evaluation of the acoustic radiation from tip vortex cavities. The discretization approaches entail the arrangement of equivalent acoustic sources for the tip vortex cavity. The acoustic radiation characteristics from the two models are modelled using the Farrassat −1A formulation of the Ffowcs-Williams–Hawkings equation (3). Initially, a verification study (Section 4) is conducted, wherein the acoustic radiation from the two discretization approaches are compared with reference to the analytical solution from Morozov (1974), for the case of harmonic surface waves propagating along an infinitely long cylinder. The extents of validity of the analytical solution are explored for various factors that are important when extending the numerical models to the case of a propeller tip vortex cavity.

The next part of the paper (Section 5) broadens the application of the numerical models to a realistic propeller tip vortex cavity through a validation study. The fluctuating tip vortex cavity geometry in the validation study is determined based on Rayleigh–Plesset equations with boundary conditions from a potential flow solution of the propeller flow, in contrast to the prescribed harmonic oscillations in the verification study. The flow solver includes the effects of sheet cavitation as well. The acoustic radiation from the realistic tip vortex cavity, using the two discretization models, is evaluated for a full-scale propeller. Eventually, a comparison with full-scale measurements is performed to ascertain the effectiveness of the FWH-based acoustic model for industrial applications. The comparison study also attempts to account for the disparities between the simulation and measurement environments, in order to quantify the degree of uncertainty one can expect when validating numerical acoustic results with full-scale measurements.

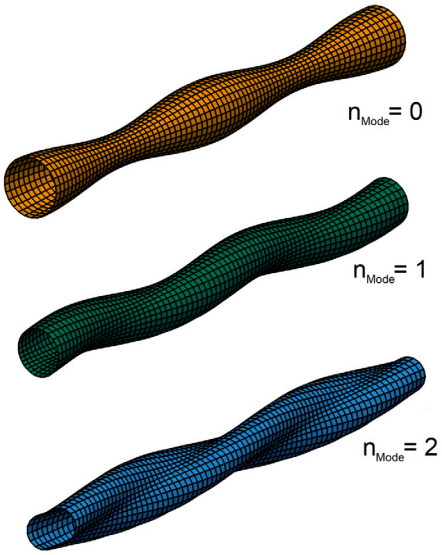

Fig. 2. Visualization of the spatial deformation of a cavitating vortex for the modes n_{Mode}=0, 1 and 2 at one instance of time.

3. Formulation of TVC acoustic radiation models

The tip vortex cavity is a dynamic vorticial structure downstream of the propeller flow, with shape and size fluctuations excited by the varying velocity and pressure field encountered by the rotating propeller blades. Numerical acoustic models of the tip vortex cavity are aimed at predicting the acoustic radiation from the dynamic cavity structure, through reasonable simplifications. Simplified, analytical models that relate the free-field acoustic radiated pressure to the cavity volume acceleration are available in the literature (Arveson and Vendittis, 2000). In this section, two such numerical models are discussed, whose practical application in acoustic radiation of cavity structures is subsequently investigated.

The three prominent mode shapes for deformation of the cavitating vortex (Bosschers, 2008) are seen in Fig. 2. The mode $n_{\text{Mode}} = 0$ (breathing mode) involves volume variations, but the axis of the vortex remains constant. The mode $n_{\text{Mode}} = 1$ (serpentine mode) leads to the displacement of the vortex centre line. The breathing and serpentine mode shapes are characterized by a circular cross-section of the vortex core. The mode $n_{\text{Mode}} = 2$ (double helix mode) leads to an elliptical shape of the vortex core. For regular cross-section cavity shapes, discounting the three-dimensional curvature, the helical structure may be idealized as an elongated, curvilinear cylinder. A cylindrical co-ordinate system is defined to better understand the geometrical properties of the tip vortex cavity, as seen in Fig. 3. The axial direction (x) of the idealized cylinder corresponds to the tip vortex trajectory, the radial direction (ξ) corresponds to the radial fluctuations of the tip vortex cavity, and the circumferential direction (θ) corresponds to shape fluctuations around the cavity axis.

The first model – Model 2D – is a two-dimensional geometrical representation of the tip vortex cavity, which can account for changes in the tip vortex trajectory, as well as cross-sectional changes of the cavity. The second model – Model 1D – is a one-dimensional model, which also accounts for changes in the tip vortex trajectory but assumes a circular shape for the cavity cross-section. Therefore, it considers periodic changes only in the size of the cavity cross-section, but not in the shape. That is to say, the assumption of axisymmetry in Model 1D can only be employed to simulate cavity deformations that adhere to mode shapes $n_{\text{Mode}} = 0$ and $n_{\text{Mode}} = 1$, whereas Model 2D is additionally able to represent the mode shape $n_{\text{Mode}} = 2$. Nevertheless, the first mode ($n_{\text{Mode}} = 0$) is believed to be the dominant, because for small, harmonic

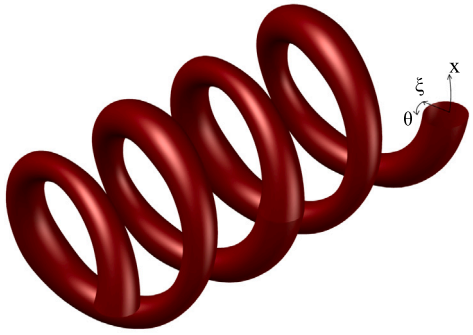

Fig. 3. Visual representation of a helical tip vortex cavity.

perturbations with low frequency, the breathing mode is the only mode contributing to far field noise (Bosschers, 2008). Both models discretize the cavity geometry into segments along the axial direction. A visual representation of the two models is provided in Fig. 4.

The discretization models also provide a framework for the definition of representative acoustic sources for the tip vortex cavity. Volumetric variation of the tip vortex cavity results in acoustic pressure waves radiated into the free-field in the form of thickness induced noise. The tip vortex cavity acoustic models are intended to approximate the radiation of the acoustic waves, by defining equivalent acoustic sources. The discretization approach in Model 2D yields an acoustic model wherein the acoustic sources are defined along the surface of the tip vortex cavity. The equivalent acoustic point sources from Model 1D are defined along the cavity axis. The equivalent source representations can be inferred from Fig. 4.

3.1. Cavity surface representation

The representation of the cavity surface is based on the idealization of the helical cavity structure into an elongated cylinder. Consider the instantaneous cavity radius, at any axial distance x from the origin, to be described by the function $\Upsilon(x,t)$. In order to numerically evaluate the cavity dynamics, the cavity surface has to be discretized into finite segments. A piece-wise cylindrical approach is used here, wherein discrete cylinders of radius $\Upsilon(x,t)$ and height $\mathrm{d}x$ are defined at every discrete interval along the x-axis (see Fig. 5). The piece-wise cylindrical approach provides sufficient accuracy with regard to the representative cavity surface area, as can be seen in Appendix A.

The volume of a cylindrical segment is obtained as $\pi\Upsilon^2\mathrm{d}x$, and its external surface area as $2\pi\Upsilon\mathrm{d}x$. In Model 2D, the cylindrical segments are partitioned into n_θ equal sub-surfaces. Therefore, the instantaneous surface area of an element is given as seen in (4).

$$\mathrm{dS}_{2D}(x,t) = \frac{2\pi\Upsilon(x,t)\mathrm{d}x}{n_\theta} \tag{4}$$

The sound radiation from the tip vortex cavities follows the same mechanism as that from a volumetric pulsation. For such a source, the source strength is proportional to the second derivative of the pulsating volume (Ffowcs-Williams and Lighthill, 1971). The simplification proposed in Model 1D is based on this relation. An equivalent spherical element with radius r_{sph} (5) is defined such that it occupies the same volume as the cylindrical segment. The surface area of the spherical element used in Model 1D is then obtained as seen in (6).

$$r_{\mathrm{sph}}(x,t) = (3/4\Upsilon^2(x,t)\mathrm{d}x)^{1/3} \tag{5}$$

$$\mathrm{dS}_{1D}(x,t) = \pi[6\Upsilon^2(x,t)\mathrm{d}x]^{2/3} \tag{6}$$

3.2. Acoustic representation

In a ship-fixed reference frame, the tip vortex cavity surface may be represented as a discretized collection of acoustic sources, defined by the Farrassat −1A integral formulation (3). The cavity surface deformation velocity ($\boldsymbol{v}_{\mathrm{def}}$) can be taken as the surface velocity ($\boldsymbol{v}$) of each discrete source, based on the following assumptions:

1. The cavity surface deformation of any piece-wise cylindrical element takes place along its radial direction. Hence, the deformation velocity is always in the direction of the normal vector, i.e. $\boldsymbol{v}_{\mathrm{def}} \cdot \hat{\boldsymbol{n}} = \dot{\Upsilon}(x,t)$.
2. The influence of the surrounding flow on the cavity surface is negligible, i.e. there is no interaction between the cavity surface and the surrounding flow.
3. There is no interaction between adjacent cavity segments. The propagation of disturbances along the cavity axis is prescribed by the flow model.

Combining these simplifications, the thickness induced noise due to the tip vortex cavity can be expressed as:

$$p_T(\boldsymbol{x},t) = \frac{\rho_0}{4\pi}\sum_{j=1}^{n_{\mathrm{ax}}}\sum_{i=1}^{n_\theta}\mathrm{dS}_j(t)\left[\frac{\dot{\boldsymbol{v}}_{ij}\cdot\hat{\boldsymbol{n}}_{ij} + \boldsymbol{v}_{ij}\cdot\dot{\hat{\boldsymbol{n}}}_{ij}}{r_{ij}|1-\boldsymbol{M}_{ij}\cdot\hat{\boldsymbol{r}}_{ij}|^2} + \frac{\boldsymbol{v}_{ij}\cdot\hat{\boldsymbol{n}}_{ij}\left(r_{ij}\dot{\boldsymbol{M}}_{ij}\cdot\hat{\boldsymbol{r}}_{ij} + c\boldsymbol{M}_{ij}\cdot\hat{\boldsymbol{r}}_{ij} - c\|\boldsymbol{M}_{ij}\|^2\right)}{r_{ij}^2|1-\boldsymbol{M}_{ij}\cdot\hat{\boldsymbol{r}}_{ij}|^3}\right]_{\mathrm{ret}}, \tag{7}$$

in the discretized form. Here, j is the index for elements along the axial direction, and i is the index for elements along the circumferential direction. Eq. (7) is valid for both Model 2D and Model 1D, with the differences summarized as follows:

- $n_\theta = 1$ for Model 1D.
- the surface area of the discrete element is represented by Eqs. (4) and (6) respectively.
- the cavity rotational velocity in Model 1D is purely in the tangential direction, and hence always orthogonal to the normal vector of the discrete elements. Therefore, for Model 1D,

  $$\boldsymbol{v}_{ij}\cdot\hat{\boldsymbol{n}}_{ij} = \dot{\Upsilon}_j. \tag{8}$$

  In the far-field, the first term in the thickness induced noise (of monopole nature) dominates the acoustic pressure. Consequently, the simplified relation equating the acoustic pressure to the cavity volume acceleration (Arveson and Vendittis, 2000) can be arrived at.
- the radiation vector, $\hat{\boldsymbol{r}}_{ij}$, in Model 2D provides a more accurate rendering of the directivity of the acoustic source, especially for closer observer points.

4. Verification of acoustic models

Numerical hydroacoustics deals with the prediction of acoustic pressure fluctuations, which are several orders of magnitudes lower than the absolute pressure field within which they are present. The nature of the problem, in terms of a relative magnitude scale, creates uncertainties for both measurements and numerical computations. Such uncertainties are extended towards validation of the numerical models with experimental measurements, and even with other numerical models. Therefore, a reliable approach to ascertain the applicability of a numerical model is through verification with an analytical solution.

Like many other similar physical problems which are extended to practical applications, tip vortex cavity acoustics also has the issue that it is difficult to obtain relevant analytical solutions. While various assumptions and simplifications are employed in analytical solutions, their relevance often deviates from the practical application. For example, the sound field radiated by simple sources (monopoles, dipoles,

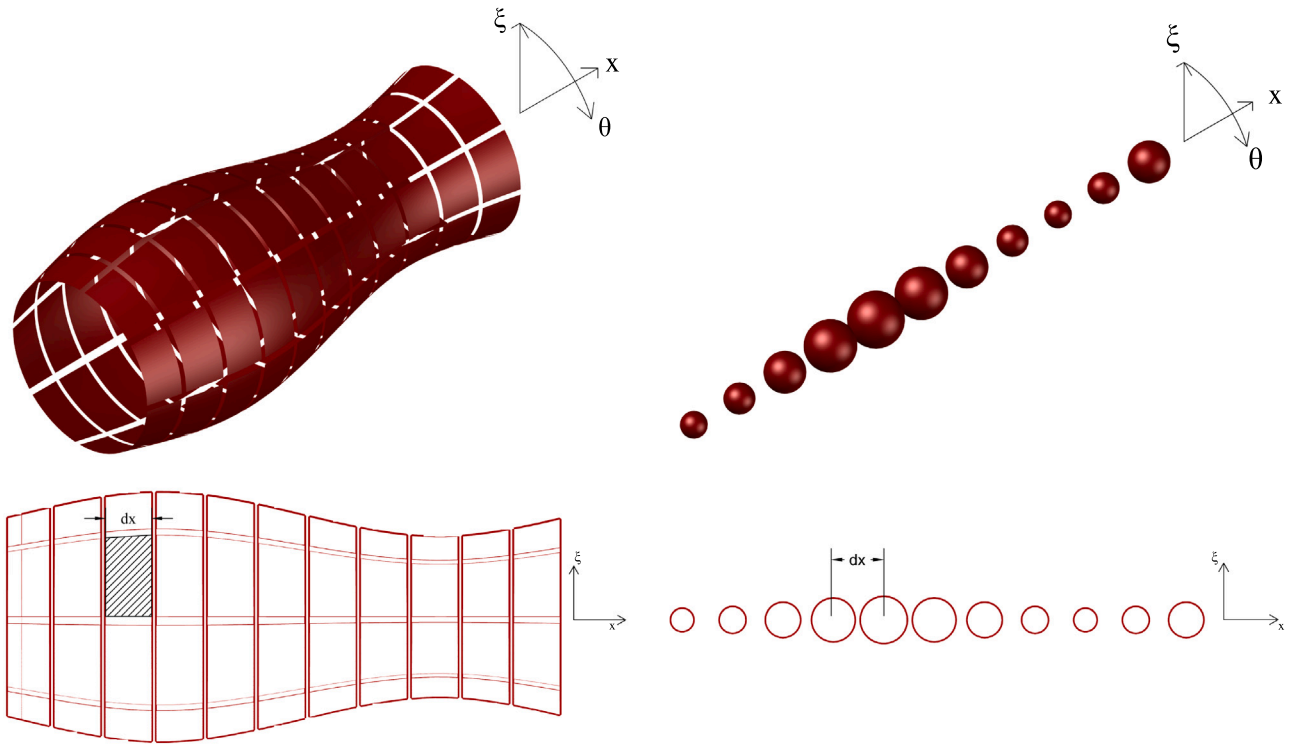

(a) Model 2D - Discrete sources around the cavity surface

(b) Model 1D - Discrete sources along the cavity axis

Fig. 4. Tip vortex cavity acoustic models: 3D isometric view (above), top view (below).

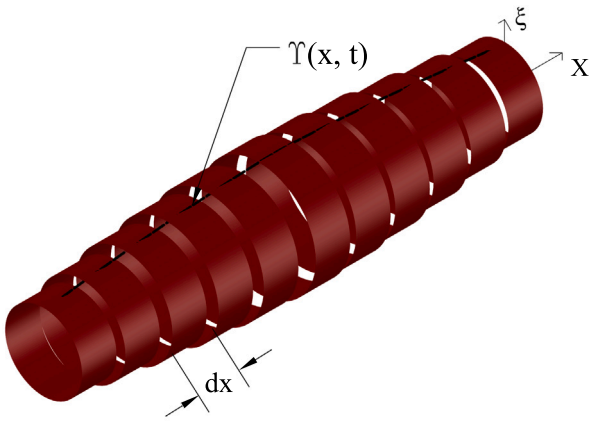

Fig. 5. Piece-wise cylindrical discretization of the idealized tip vortex cavity.

quadruples, etc.) can be analytically expressed, but these formulations assume an infinitesimally small size of the sound source in comparison to the sound wavelength. The finite size and shape of the sound source can be accounted for in the analytical solution for the acoustic radiation of a pulsating sphere within a static medium (Urban, 2002). Such verification studies have been included while developing numerical acoustic models for noise from propeller blades (Göttsche, 2020). However, the geometrical shape variation in the pulsating sphere case does not closely resemble that in the case of a tip vortex cavity. Analytical solutions pertaining to long cylinders are more relevant in the case of a tip vortex cavity. At longer distances to the observer point, the pulsating sphere geometry behaves essentially as a monopole source; whereas, more interaction is expected between the elements discretizing a long cylinder.

Existing literature pertaining to analytical solutions related to acoustics of cylindrical shapes is briefly discussed in Section 2.2. Among these, the analytical solution proposed by Morozov (1974) is used to benchmark the proposed acoustic models in this paper. The aim of the verification study is to determine the spatial and temporal resolution required to accurately estimate the known analytical solution through the numerical models. The results are discussed taking into account the limitations of the analytical solution, and the outcome sheds light on the requisite numerical resolution while modelling propeller tip vortex cavities.

4.1. Description of analytical solution

The analytical solution from Morozov (1974) is based on a theoretical analysis of the acoustic emission from cavitation line vortices. The geometry of the line vortex is described by harmonic waves on an axisymmetric, cylindrical cavity, wherein the fluctuation radius is defined by a sinusoidal function. The important results are summarized in a visual representation of the analytical case in Fig. 6.

Consider harmonic oscillations of amplitude $\tilde{\Upsilon}$ on the surface of a finite cylindrical cavity of length L_x and radius $\bar{\Upsilon}$. The surface of the oscillating cylinder is given by $\Upsilon = \bar{\Upsilon} + \tilde{\Upsilon} e^{i(\alpha x - \sigma t)}$. Here, α is the wave number of the surface propagating wave, and σ is its frequency for the breathing mode ($n = 0$). The surface wave propagates with a velocity c_x and wavelength λ_x, such that $c_x = \frac{\sigma}{2\pi}\lambda_x$. Morozov (1974) proposed an analytical solution for the acoustic radiated pressure in a medium with density ρ_0 for such a cylindrical cavity, when $L_x \to \infty$. The complex acoustic pressure at a receiver point that is located a radial distance r from the cylinder axis, is given by:

$$\tilde{p} = p_{\text{ref}} e^{i(kx - \sigma t)}, \quad \text{where } p_{\text{ref}} = \rho_0 \tilde{\Upsilon} \frac{\sigma^2}{\beta} \frac{H_0(\beta r)}{H_0'(\beta \alpha)} \tag{9}$$

Here, k is the acoustic wave number and $\beta = \sqrt{k^2 - \alpha^2}$. H_0 refers to the Hankel function of the first kind of order zero, and H_0' its derivative.

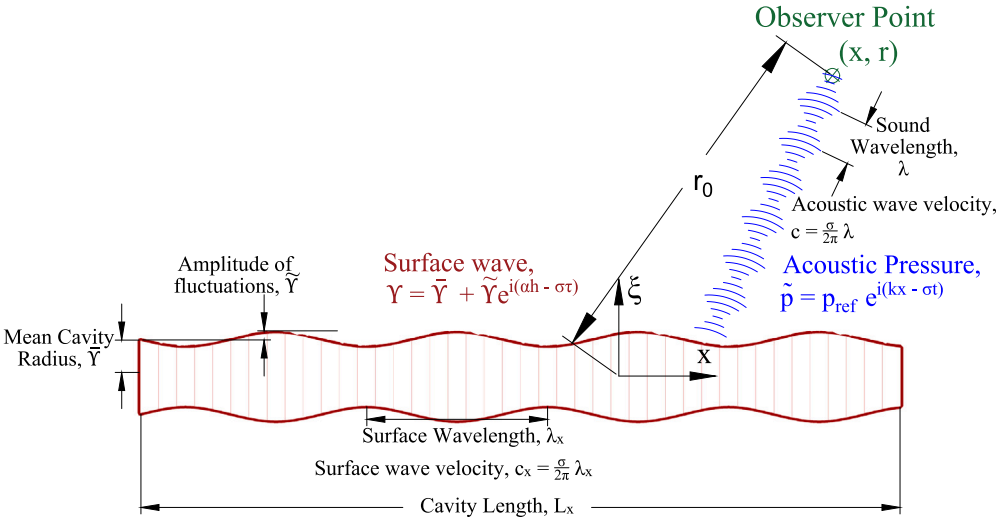

Fig. 6. Description of the parameters used in the Morozov analytical case.

4.2. Convergence study

When simulating the effect of a surface propagating wave, such as in the case of the Morozov analytical solution, it is self-evident that the accuracy of the solution depends on the accuracy with which the wave is captured within the simulation — both in the spatial and the temporal domains. The convergence study is aimed at understanding the impact of such numerical resolution parameters. In this paper, the numerical resolution parameters are defined in terms of non-dimensional parameters. The defining parameter in the temporal domain is the number of time steps per surface wave period (n_t). The axial spatial resolution is defined for both models by the number of elements per surface wavelength (n_x). Model 2D has an additional spatial resolution parameter — the number of circumferential elements around the cavity axis (n_θ).

The baseline case for the convergence study is based on the exemplary special case provided in Morozov (1974). This case considers the acoustics of a cylindrical, vapour-filled cavity with 3 mm mean radius. The angular velocity of rotation is determined from the Bernoulli equation, by assuming the free-stream pressure to the atmospheric pressure. The flow Mach number, defined by the ratio of the linear velocity of rotation at the mean cavity radius to the speed of sound in the medium, is calculated as 0.0093. The corresponding frequency of the breathing mode is 320 Hz. The amplitude of radial fluctuations considered is 1% of the mean radius. While the proposed theoretical solution is for an infinite cavity length, the verification study considers a finite cavity length of 1000 m. The surface propagating wave has a wavelength of 50 m, which is sufficient to fulfil the infinite length assumption ($L_x \gg \lambda_x$), and the acoustic emission condition ($c_x > c$) proposed by Morozov (1974). Physical constants, such as the surrounding fluid density and speed of sound, are defined as 1000 kg/m^3 and 1500 m/s respectively. The observer point is located in the cavity centre plane ($x = 0$) and 10 m radially away from the cavity axis. The convergence behaviour is assessed based on the relative error of the acoustic pressure amplitudes between the simulated and the analytical solutions.

Firstly, a convergence study is conducted on the circumferential resolution of Model 2D, in order to identify the suitable resolution required for the rest of the evaluation. Fig. 7 shows the convergence behaviour for varying circumferential resolutions, wherein each curve corresponds to a fixed axial and temporal resolution. The axial resolution n_x and the number of time steps at the observer n_t were varied from 0 to 100 in steps of 5, but only curves for selected values are shown in the plot. Besides the resolutions, the angular position of the observer was varied to cover 10 equally spaced angles within $2\pi/n_\theta$. The error

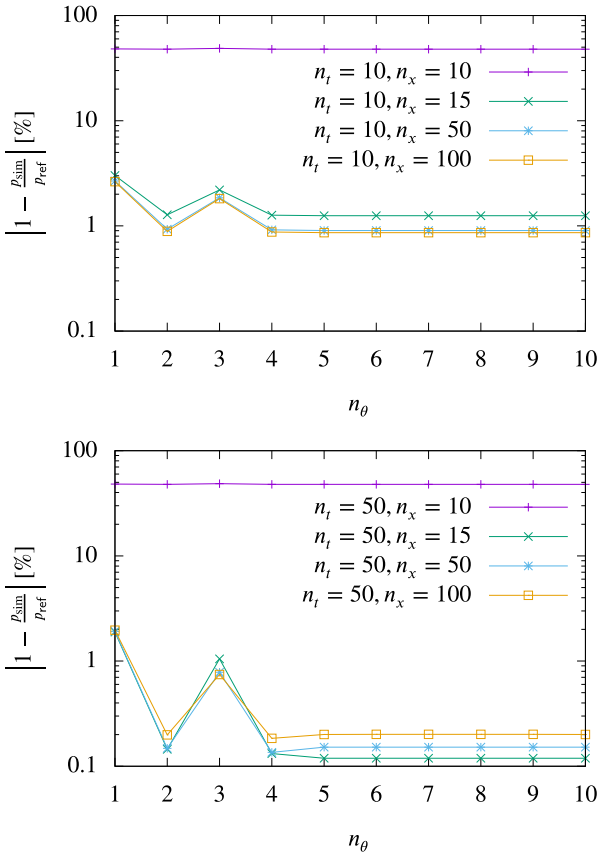

Fig. 7. Grid dependency study for circumferential resolution of Model 2D.

discussed is the maximum error. It is observed that no considerable improvement in the simulated solution is obtained by increasing the circumferential resolution greater than 5. The maximum deviation of the simulated solution from the analytical solution, for $n_\theta \geq 5$ and $n_x \geq 15$, is 1.3%. Due to the negligible change for higher resolutions, a circumferential resolution of $n_\theta = 5$ is considered sufficient for all further studies.

With the circumferential resolution fixed ($n_\theta = 5$), the rest of the convergence study is conducted to determine the impact of varying the

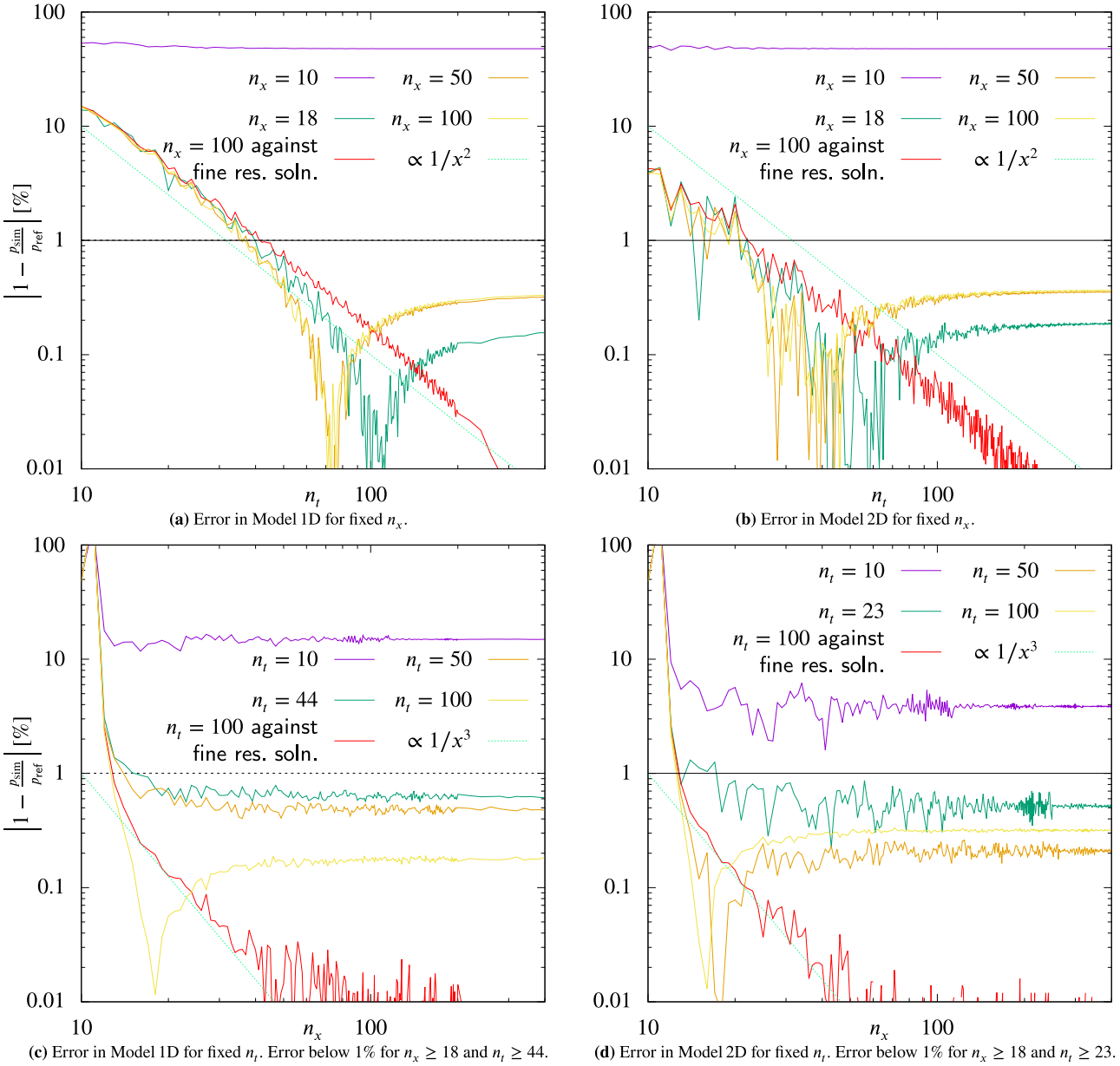

(a) Error in Model 1D for fixed n_x.

(b) Error in Model 2D for fixed n_x.

(c) Error in Model 1D for fixed n_t. Error below 1% for $n_x \geq 18$ and $n_t \geq 44$.

(d) Error in Model 2D for fixed n_t. Error below 1% for $n_x \geq 18$ and $n_t \geq 23$.

Fig. 8. Convergence of simulation w.r.t. the analytical solution. The red lines indicate the convergence behaviour towards the finest resolution solution, instead of the analytical solution used for the other curves.

axial and temporal resolutions. Simulations of the analytical case are performed for all integer combinations of n_x and n_t between 10 and 200. To assess the convergence behaviour in space and time separately, the errors are plotted separately. The convergence behaviour is clearer from the red curves, in which the reference solution is the respective fine resolution solution. Figs. 8(a) and 8(b) show the convergence behaviour in time for models 1D and 2D respectively. Both models show approximately second order convergence in temporal resolution, as indicated by the proportionality line. In Figs. 8(c) and 8(d), the respective convergence behaviours with respect to axial resolution are shown. Both the models show a rapid convergence to a steady error value, much faster than that for the temporal resolution. Thereafter ($n_x > 12$), an approximate third order convergence is observed. Only selected curves are plotted on Fig. 8 to manage the compactness of the plot.

It may be noted that the simulated solutions for both models do not converge exactly to the analytical solution, even for fine resolutions. For both models, the converged solution shows approximately 0.3% error with respect to the analytical solution. This is also the reason why a local minima is observed. The influence of critical parameters that contribute to this discrepancy is investigated in the sensitivity study in the following sub-section. The results from the convergence study are used to determine appropriate temporal and spatial resolutions for the sensitivity study.

The convergence behaviour for both models are independent of each other, and hence the appropriate resolutions chosen are different for each model. The criteria employed is that the relative error is within 1%. For Model 1D, axial resolutions beyond 18 and temporal resolutions beyond 44 do not significantly improve the error. For Model 2D, the appropriate axial resolution is 18 (coincidentally), and the appropriate temporal resolution is 23. Curves corresponding to these chosen resolutions are indicated in Fig. 8. The progression of the curves for the error below the horizontal 1% error line indicates that the relative error stays below 1% for resolutions finer than the chosen ones.

4.3. Sensitivity study

Morozov (1974) states that in order to equate a long finite length cavity to an infinite length cavity, the following four quantities have to be small as compared to the cavity length — the observer point location r_0, the surface wavelength λ_x, the sound wavelength λ and the amplitude of fluctuations $\tilde{Y}$. A sensitivity study is undertaken to understand the influence of these parameters on the simulated solution. The results of the sensitivity study are presented in Figs. 9 to 11. The vertical axis of each plot is the ratio between the simulated acoustic pressure amplitude and the analytical solution for the corresponding case.

Fig. 9 shows the variation of the simulated solution when the observer location is changed radially, as well as axially. For variations along the radial direction, the observer point is located at the centre of the cavity length (i.e. $x = 0$, with the cavity extending from $x = -L_x/2$ to $x = +L_x/2$). For variations along the axial direction, the observer point is located at a radial distance 10 m away from the cavity axis. The fluctuations in the pressure amplitude ratio are likely due to the retarded time interpolation algorithm used in the FWH method. Hence, the sensitivity of the solution to the observer point location is best understood by focusing on the envelope of the curves.

As expected for large observer point distances, the analytical solution is no longer valid, as shown by the high deviations of the pressure amplitude ratio. When the observer point location satisfies

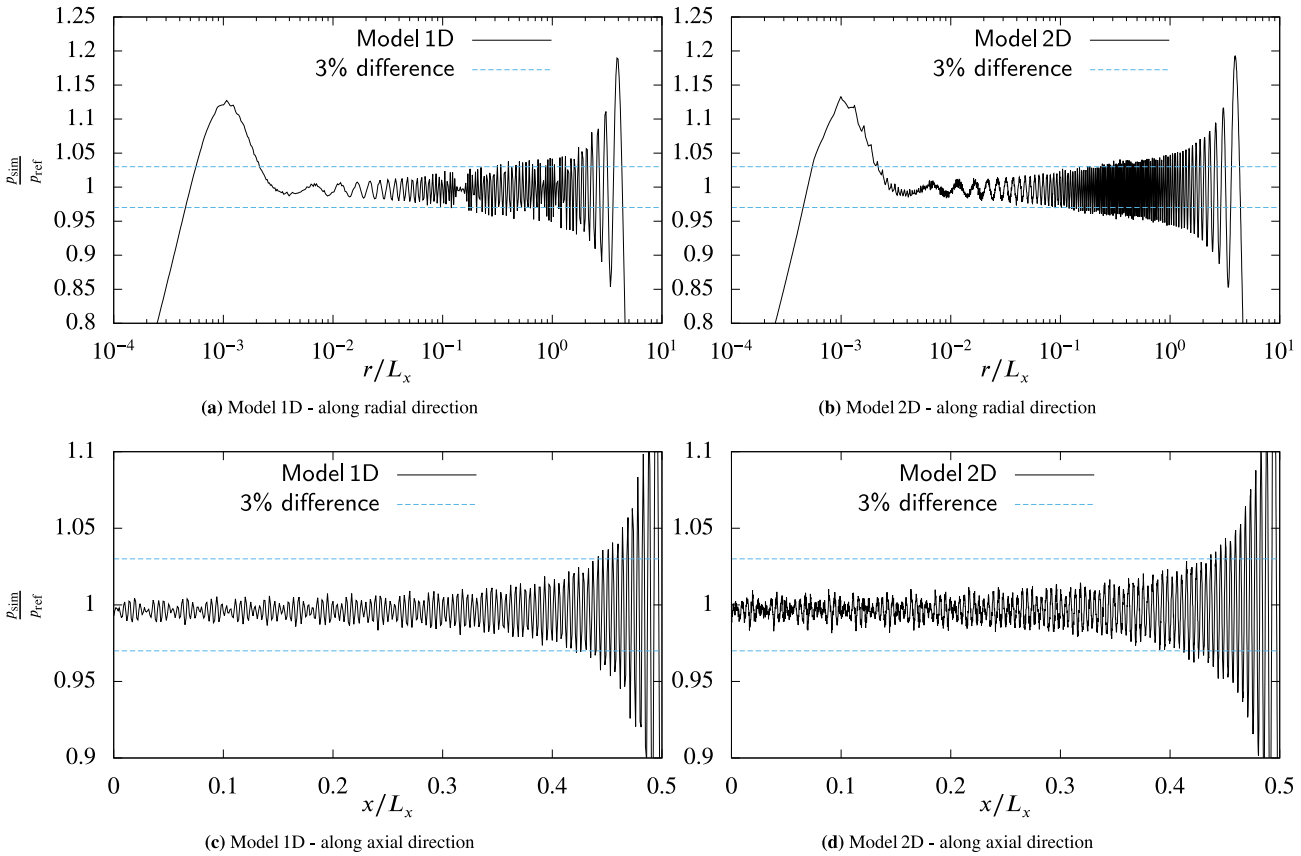

(a) Model 1D - along radial direction

(b) Model 2D - along radial direction

(c) Model 1D - along axial direction

(d) Model 2D - along axial direction

Fig. 9. Acoustic amplitude over different observer positions.

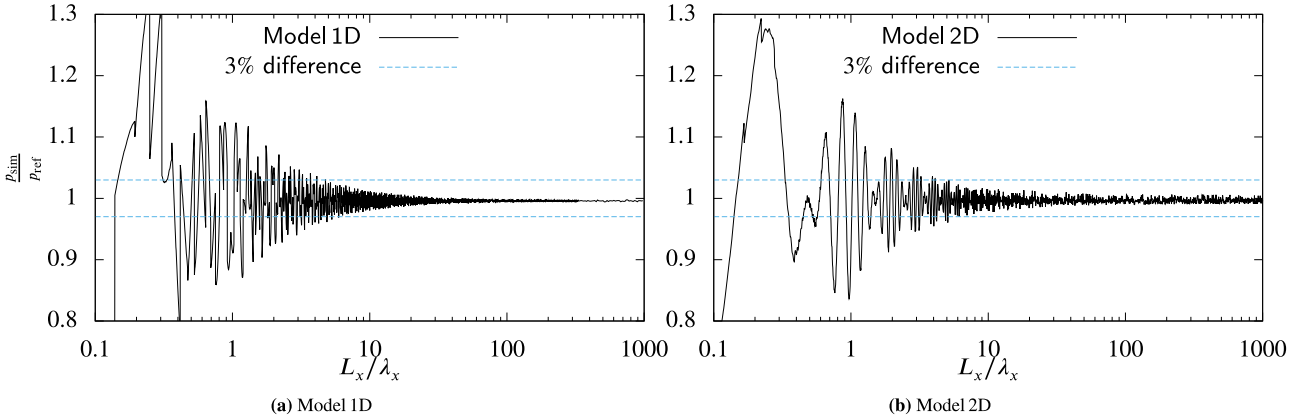

(a) Model 1D

(b) Model 2D

Fig. 10. Influence of cavity length L, for fixed observer point (x=0, r=10 m).

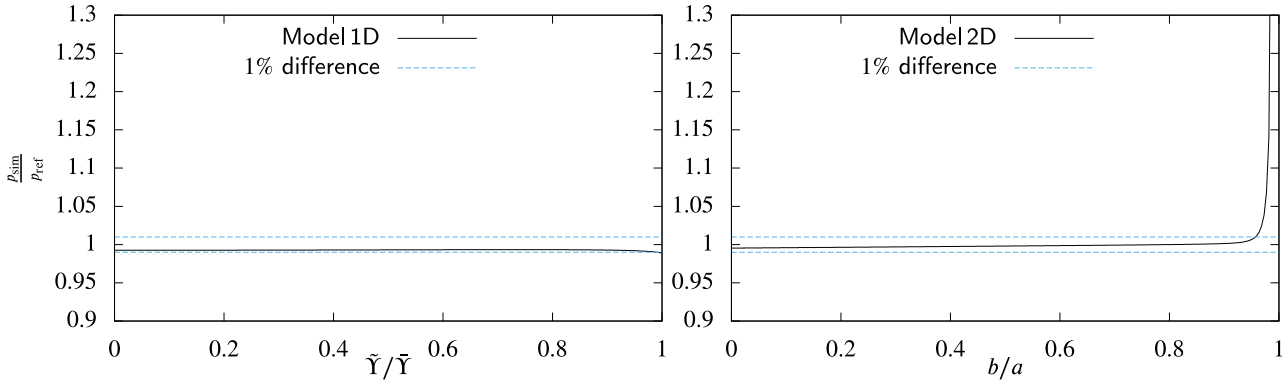

(a) Model 1D **(b)** Model 2D

Fig. 11. Influence of amplitude of fluctuations, at fixed observer point (x=0, r=10 m).

the analytical case assumption $r_0 \ll L_x$, the difference is within 3%. As the observer point gets closer, the deviation from the analytical solution decreases, thereby highlighting the impact of this necessary assumption for the analytical case. However, for observer points whose radial distances are very close to the cavity centre ($r/L_x < 3 \times 10^{-3}$), there is a larger deviation from the analytical solution. This happens due to a limitation of the discretization, wherein the solution close to the elements are generally unreliable. The general rule of thumb is that this limiting distance is approximately equal to one element length. For the sensitivity study in Fig. 9 with an axial resolution of $n_x = 18$, the ratio of the element sizes to the cavity length is 2.78×10^{-3}, which duly matches this limiting criterion.

Similar trends were observed while undertaking the sensitivity study by changing the cavity length in Fig. 10. As the cavity length gets larger, the simulated solutions have better agreement with the analytical solution, with reduced fluctuations of the amplitude ratio. The performance of the acoustic models for shorter length cavities is also appreciable. The variation from the analytical solution stays within 3% for cavity lengths as low as 5 times the surface wavelength. This is an encouraging outcome for propeller tip vortex cavity cases, where it is unfeasible to model a long tip vortex cavity. It should also be noted that for lower cavity lengths, the limitation is on the analytical solution. The acoustic models may still be valid, but this cannot be ascertained using the current analytical solution case.

Another critical parameter when extending the simplified analytical case to the practical case of propeller tip vortex cavities is the relative amplitude of fluctuations on the cavity surface. This is represented by the ratio of the fluctuation amplitude to the mean radius $\tilde{Y}/\bar{Y}$, and the corresponding sensitivity study is provided in Fig. 11. Even though the analytical solution was derived for relatively small amplitude of fluctuations ($\tilde{Y} \ll \bar{Y}$), practical tip vortex cavities encounter much higher amplitudes. The surface wave amplitude ratio ($\tilde{Y}/\bar{Y}$) can be as high as 1, resulting in the collapse of the cavity and leading to tip-vortex splitting. This is the main motivation to investigate how the models behave for high amplitude ratios. It is encouraging to see that both models show good and consistent agreement with the analytical solution, for amplitude ratios as high as 0.95. The asymptotic behaviour of both models close to cavity collapse are different due to the nature of their definition. Model 2D retains the cylindrical shape of the cavity segments; therefore, higher amplitude fluctuations can result in a greater degree of inaccuracy in the definition of the individual elements. Model 1D assimilates only the volume change, which is an integrated quantity, and hence the consistency in behaviour persists much closer to the cavity collapse scenario.

Despite accounting for the parameter limits that assure an infinite length cavity, the simulated solutions do not seem to converge exactly to the analytical solution. The reason for this discrepancy could not be identified. Nevertheless, with the converged solution only showing a 0.3% deviation, further effort is not poured into investigating the reason for the small discrepancy. The deviation is still within acceptable limits, and sufficient to continue further investigations for the propeller tip vortex cavity acoustics.

4.4. Summary of verification study

The general conclusion from the verification study is that the proposed acoustic models show consensus for the analytical cases considered. The limitations of the analytical solution, especially with regards to extending the application of the infinite cylindrical cavity case to a finite tip vortex cavity with high fluctuation amplitudes, have been explored in the sensitivity study. The results from the sensitivity study suggest that the acoustic models are expected to provide acoustic pressure amplitudes within 3% difference, for harmonic fluctuations on a tip vorticial structure that resembles a long cylinder.

It is also important to understand the significance of the investigated parameters with respect to propeller tip vortex cavities. The proximity of the observer point to the discrete elements is a limitation in flow solutions that are based on the panel method. The sensitivity study provides a quantitative estimate to this distance (see Fig. 9), with the observation that there is no considerable deviation from the analytical solution for distances as close as 1/1000th of the simulated cavity length. This also roughly corresponds to the length of one discrete element. The requirement of the minimum cavity length to accurately represent the surface waves is also investigated in the sensitivity study. A good rule of thumb would be to have the simulated cavity be as long as five times the wavelength of the smallest frequency wave, although smaller lengths may suffice. Conclusive recommendation on the tip vortex cavity length cannot be made from the current sensitivity study unfortunately, due to limitations in the analytical solution. The high amplitude of fluctuations in propeller tip vortex cavities is a distinct constraint when compared to the small perturbations in analytical cases. The sensitivity study in this regard (Fig. 11) points towards an evident validity of the application of the numerical discretization models for large amplitude fluctuations.

5. Case study for propeller tip vortex cavity

The verification study performed in Section 4 serves as a primary step in determining the suitability of the acoustic models to predict the acoustic noise generation of a pulsating volume source. The next step is to determine the suitability of the method for propeller tip vortex simulation applications. While the cavity geometry and oscillations in the verification study were prescribed, the case study includes a representative geometry of the propeller tip vortex cavity obtained

through numerical simulations. The following key features differentiate a propeller tip vortex cavity geometry from the analytical description of the breathing mode harmonic waves used in the verification study:

- The tip vortex cavity geometry is generally not axisymmetric. It is a combination of axisymmetric and non-axisymmetric mode shapes, as seen in Fig. 2.
- The amplitude of radial fluctuations for a tip vortex cavity is usually of the order of magnitude of the mean radius, i.e. $\tilde{\Upsilon} \ll \bar{\Upsilon}$ is not generally valid. In high velocity flows, this can even result in tip vortex cavity splitting and coalescence, which cannot be described completely by the linear theory of harmonic oscillations.
- The simplification of the three-dimensional tip vortex cavity geometry into two-dimensions (in Model 2D) and one-dimension (in Model 1D), can lead to loss of geometric information such as tip vortex elongation.
- The location of the observer point for propeller noise prediction cases is usually far away, beyond the distance assumption of the Morozov model.
- In practice, the propeller tip vortex cavity dissipates into the flow field after a finite distance, as opposed to the infinite length cylindrical cavity in the analytical case.

Nevertheless, the simplified models provide reasonable estimates for the prediction of the acoustic noise from tip vortex cavities. In order to truly evaluate the impact of these simplifications, a case study has to be performed with a representative ship propeller tip vortex geometry. This section describes the application of the acoustic models for a standard propeller geometry, including a comparison with the full-scale noise measurements.

5.1. Numerical model of the cavitating propeller flow

For simulating the unsteady propeller flow including the effects of developed sheet and tip vortex cavitation, ESPPRO, the in-house panel code of DTU (Technical University of Denmark), is used. A brief outline of the potential flow model in ESPPRO and how it incorporates sheet cavitation is provided in Appendix B. The applied model for developed tip vortex cavitation is based on ideas of Szantyr (2006) and Kanemaru and Ando (2015). The model is described in detail by Berger (2018); information on the current implementation in ESPPRO is given by Mirsadraee (2019).

The basic principle of the tip vortex cavitation model is depicted in Fig. 12. The model is based on the assumptions of a cylindrical cavity in the core of the tip vortex. Further, the cavitating tip vortex is split into a large number of segments j, each of them is associated with a position, the cavitation radius Υ_j and the circulation Γ. In every time step, a new segment is initialized at the propeller tip and the already existing segments are shifted in the downstream direction. Due to the roll-up process of the sheet of trailing vorticity, the circulation attributed to a segment is not constant. This means the circulation along the vortex axis changes, it grows from an initial value Γ_{ini} to a final value once it has reached a certain distance from the blade tip. In order to estimate the growth of circulation for a segment j, the distribution of circulation bound to the blade is analysed at the time where the segment is created. For the initial circulation Γ_{ini}, the blade circulation at a radial position of approximately 90% of the propeller radius is assumed, i.e. the initial circulation is a fraction of the maximum bound circulation Γ_b, hence: $\Gamma_{\mathrm{ini}} = \gamma_{\mathrm{ini}}\Gamma_b$. As the segment travels downstream, the circulation is increased until it reaches Γ_b. A semi-empirical function is used here, since ESPPRO does not include details of the roll-up process. The segments are shifted downstream at every time-step of propeller rotation.

Since every segment is treated in the same manner, the index j is omitted from now on. In order to calculate the unsteady cavitation radius Υ of a segment, the two-dimensional variant of the Rayleigh–Plesset equation (Franc and Michel, 2005) is used:

$$\left(\Upsilon\ddot{\Upsilon} + \dot{\Upsilon}^2\right)\ln\left(\frac{\Upsilon_D}{\Upsilon}\right) + \frac{\Upsilon^2\dot{\Upsilon}^2}{2}\left(\frac{1}{\Upsilon_D^2} - \frac{1}{\Upsilon^2}\right) = \frac{1}{\rho_0}\left(p_c - p_{\mathrm{vtx}}\right), \tag{10}$$

where

$$p_c = p_v + p_{g0}\left(\frac{\Upsilon_{\mathrm{eqm}}}{\Upsilon}\right)^{2n_{pt}}, \quad p_{\mathrm{vtx}}(\Upsilon) = p_D - \rho\int_{\Upsilon}^{\Upsilon_D}\frac{u_\theta^2}{\xi}\mathrm{d}\xi. \tag{11}$$

Here, p_c is the pressure inside the cavity, which depends on the vapour pressure p_v of water and the partial pressure $p_{g0}\left(\Upsilon_{\mathrm{eqm}}/\Upsilon\right)^{2n_{pt}}$ of non-condensable gases with the polytropic index $n_{pt} = 1$. Furthermore, p_{vtx} describes the influence of the circumferential flow u_θ around the cavitating core; p_D is the ambient pressure far away from the vortex axis at $\xi = \Upsilon_D$, the outer domain radius, which cannot be set to infinity (Berger, 2018). The initial cavity radius is assumed to be equal to the equilibrium cavity radius (Υ_{eqm}), which implies that its first and second derivatives are zero in the initial condition.

A Batchelor vortex model is applied to approximate the circumferential flow around the vortex core:

$$u_\theta(\xi) = \frac{\Gamma}{2\pi\xi}\left[1 - \exp\left(\frac{-\beta_{\mathrm{vtx}}\xi^2}{r_{\mathrm{vc}}^2}\right)\right], \tag{12}$$

with the segment's circulation Γ and $\beta_{\mathrm{vtx}} = 1.256$. The viscous core radius r_{vc} is related to the boundary layer thickness on the lifting surface (Arndt, 1995). The circumferential flow around the vortex core does not directly interact with the noise generating mechanism, but its impact is manifested through variations of the cavity segment radii (Υ) in Eq. (10).

5.2. Definition of test cases

As part of the SONIC project (European Commission, 2013), full-scale measurements were undertaken on the Princess Royal vessel, off the north east coast of England. The noise measurements in the narrowband (1 Hz band), showcasing the tonal noise, are extracted from literature (Brooker and Humphrey, 2016; Humphrey et al., 2015). Two operating conditions, for which narrowband power spectral density values are available, are used in the validation study. Details of the two operating conditions are provided in Table 2. These experimental results have previously been used in the literature to validate the numerical prediction of tip vortex cavitation (Yilmaz et al., 2020), as well as for acoustic predictions (Göttsche, 2020).

The potential flow simulations are performed using the nominal wakefield for the Princess Royal propeller, which can be found in Tani et al. (2019). The simulation uses the full-scale propeller blade geometry, with computational settings as listed in Table 1. ESPPRO simulation results displaying the extent of sheet cavitation for both operating conditions are shown in Fig. 13. The extent of sheet cavitation is comparable to that observed from the full-scale trials (Turkmen et al., 2017b), as presented in Fig. 14. Slight underprediction in the numerical

Table 1
ESPPRO simulation settings.

Parameter	Value
Propeller diameter	0.75 m
Propeller draft at hub centre	1.4 m
Atmospheric Pressure	1.03×10^5 Pa
Vapour saturation pressure	1669 Pa
Surface tension coefficient	0.07416 N/m
Fluid density	1025.9 kg/m^3
Blade mesh density (spanwise × chordwise)	25 × 30
Simulated number of revolutions	8
Angular time step	0.5°

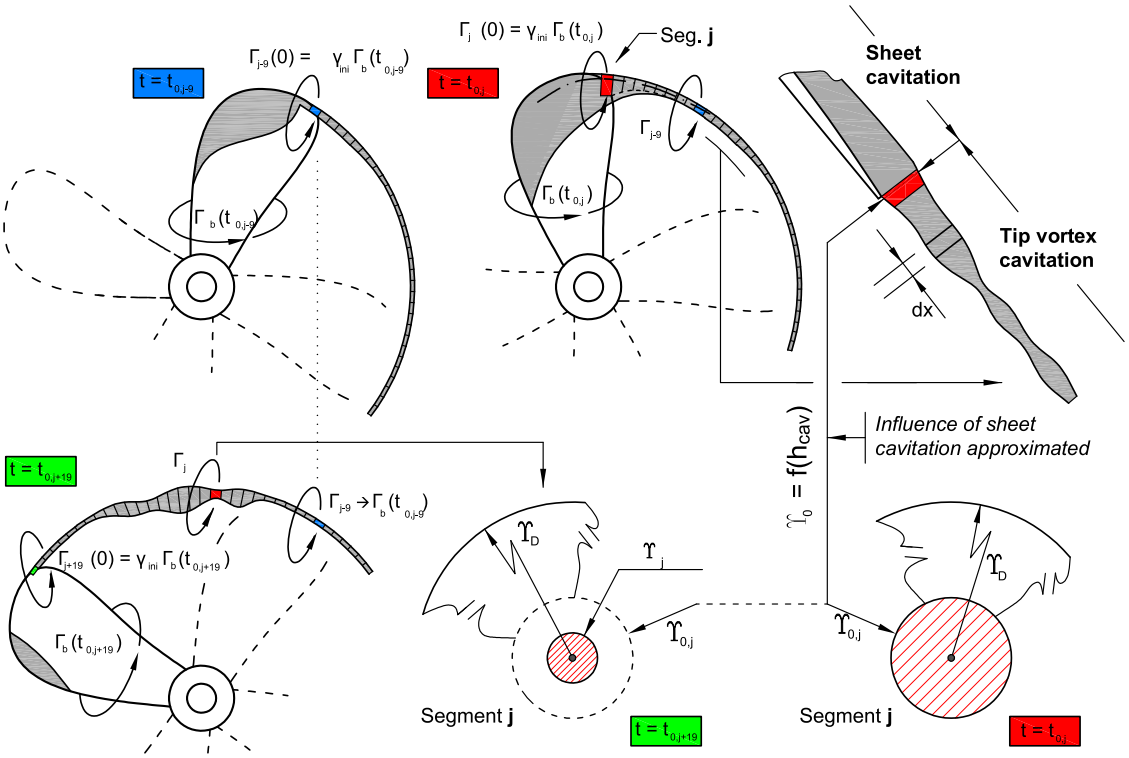

Fig. 12. Segmentation scheme of the propeller tip vortex cavitation model; influence of sheet cavitation on the dynamic behaviour of tip vortex cavitation.

Table 2
Summary of operating conditions used in the validation study.

Parameter\Case ID	1200RPM	1500RPM
Propeller speed, n [rps]	11.37	14.29
Ship speed, V_s [knots]	9.35	11.45
Advance ratio, J	0.490	0.462
Mean thrust coefficient, K_T	0.1936	0.2040
Mean torque coefficient, K_Q	0.0276	0.0288
Cavitation number, σ_n	3.10	1.96
Blade Passing Frequency [Hz]	56.84	71.43

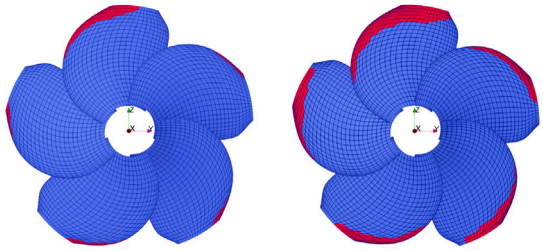

(a) 1200 RPM **(b)** 1500 RPM

Fig. 13. Sheet cavitation pattern from ESPPRO simulations. Red indicates discrete panels where sheet cavitation is predicted.

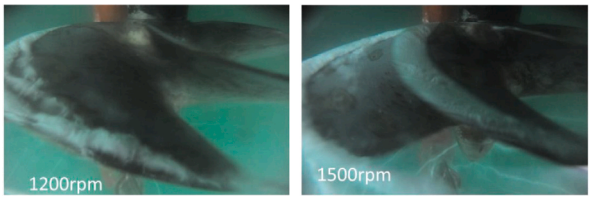

Fig. 14. Full-scale observations.
Source: Turkmen et al. (2017b).

model may be attributed to the inaccuracies in recreating the sea-trial environment, e.g. hull-propeller interaction, shaft inclination, presence of water waves.

The acoustic computation uses the blade surface pressure distribution, sheet cavity thickness data and tip vortex cavity radius from the last completed revolution. The thickness induced and loading induced noise contribution due to blade rotation is calculated based on the Farrassat −1A formulation of the Ffowcs-Williams–Hawkings equation (Eq. (3)). The presence of the sheet cavities results in additional surface velocities along the blade normal direction. The thickness induced noise due to the cavity acceleration is taken as the acoustic contribution of the sheet cavity. The contribution of tip vortex cavities is estimated independently using the acoustic models presented in Section 3. The instantaneous time history of each tip vortex cavity segment, along with the tip vortex trajectory, are the inputs used in the acoustic models. The acoustic calculations are performed in the free-field, without considering any reflecting boundaries, as the main focus is on evaluating the relative performance of the tip vortex acoustic models.

The observer point (hydrophone) is located 45 m deep and 100 m abreast of the ship centre-line. Being relatively deep compared to the other hydrophone locations, the effects of free-surface reflection are expected to be lower at this point. The evaluated sound pressure level (in dB, re 1 μPa) is converted into source levels (in dB, re 1 μPa^{2}m^2), assuming a power source with spherical spreading. The source levels are compared to the narrowband radiated noise levels provided in Humphrey et al. (2015). Since the acoustic models do not include any broadband noise phenomena and since the acoustic signals are assumed to be periodic, only a comparison of the blade harmonic noise levels is relevant. Hence the harmonic results from the numerical models are indicated as points.

5.3. Tip vortex cavitation noise spectrum

Tip vortex cavitation generates noise through impulses which are random in time of occurrence, amplitude and duration (Ross, 1976). The associated noise spectrum is a continuous broadband spectrum with acoustic energy distributed over a large range of frequencies, but still showing a broad spectral peak corresponding to the natural frequency of volumetric pulsations of the cavity. This can be seen in the pressure amplitude spectrum in Fig. 1. The flow model as well as the acoustic models used in the numerical prediction do not include statistical description of the random cavity radius fluctuations. However, the 'frequency hump' in the typical tip vortex cavitation noise spectrum can be evaluated.

5.3.1. Calibration of the flow model

The hydrodynamic model for the tip vortex cavity is based on the definite integral solution to the two-dimensional Rayleigh–Plesset-like equation (Eq. (10)) describing the oscillation of a cylindrical cavity inside a larger cylindrical domain. The finite value of the domain radius also affects the dominant frequency range of the tip vortex cavity fluctuations. Order-of-magnitude estimates of mathematical equations relating the domain radius (Υ_D), equilibrium cavity radius (Υ_{eqm}) and the tip vortex centre frequency are found in the literature (Berger, 2018).

In Fig. 15, the influence of the domain radius on the source level spectrum is shown for the acoustic simulation of the tip vortex cavity of a single blade, for the 1200RPM case. The results are only plotted for a selected few values of $\Upsilon_D/\Upsilon_{eqm}$, to manage the readability of the plot. Similar to what is expected from such a spectrum (see Berger, 2018; Bosschers, 2018a, for similar spectra), there exists a range of frequencies over which the acoustic behaviour is dominant. This 'frequency hump' is evidently dependent on the value of the domain radius chosen.

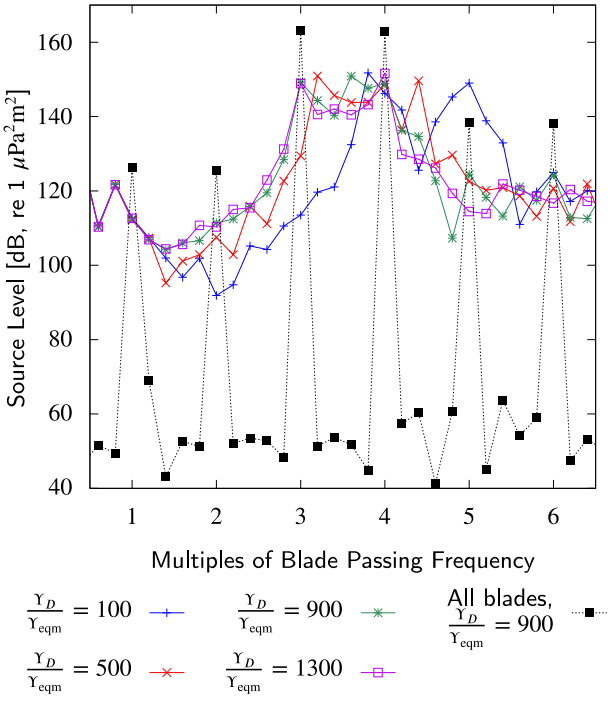

Fig. 15. Influence of domain radius on tip vortex cavity acoustic spectrum. Solid lines represent the tip vortex cavity acoustic source levels for single blade passage. Dashed black line shows the source levels when all blades are included, with $\Upsilon_D/\Upsilon_{eqm} = 900$.

Since the domain radius is not determined by the flow condition, it essentially becomes a tuning parameter for the acoustic models. For the present validation study, a domain radius ratio ($\Upsilon_D/\Upsilon_{eqm}$) of 900 is chosen based on the relative agreement of the noise harmonics with the experimental results for the 1200RPM case. Subsequently, the same value is chosen for the other operating condition.

5.3.2. Spectral peak characteristics

Proportionality relationships between the spectral peak and blade loading parameters can be obtained by order-of-magnitude estimations (Bosschers, 2018a; Berger, 2018). For the current evaluation, the semi-empirical formulations proposed in chapter 7 of Bosschers (2018a) are used, i.e.

$$\frac{f_{peak}}{f_{bp}} \propto \frac{\sigma_n}{\overline{\Upsilon}/D} \propto \frac{\sigma_n}{K_T}, \tag{13}$$

$$SL_{peak} \propto 20\log_{10}\left(\frac{\overline{\Upsilon}}{D}\right)^{\kappa_1} \propto 20\log_{10}\left(\frac{K_T}{\sqrt{\sigma_n}}\right)^{\kappa_1}, \tag{14}$$

where f_{peak} is the centre frequency of the spectral hump, SL_{peak} is the source level at the spectral peak, and κ_1 is an empirical exponent. These

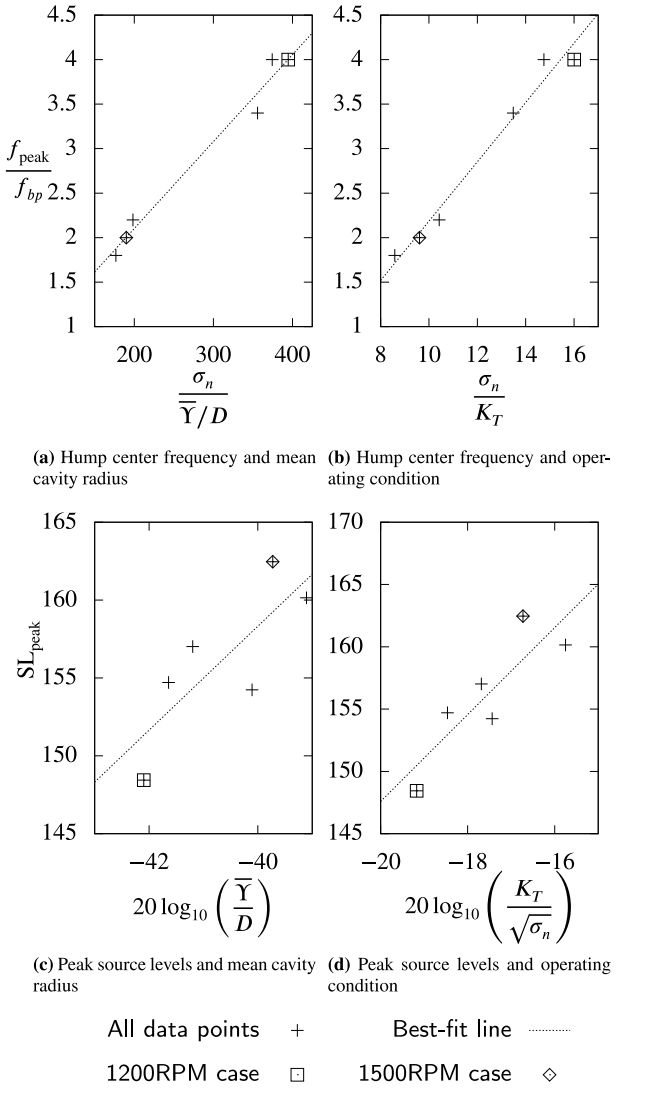

(a) Hump center frequency and mean cavity radius **(b)** Hump center frequency and operating condition

(c) Peak source levels and mean cavity radius **(d)** Peak source levels and operating condition

Fig. 16. Verification of the tip vortex cavity numerical predictions through proportionality relationships. The results are from acoustic simulations of a single blade, using Model 1D.

Table 3
Regression analysis coefficients associated to Fig. 16.

	Fig. 16(a)	Fig. 16(b)	Fig. 16(c)	Fig. 16(d)
Slope	0.0098	0.3332	3.3371	3.4892
R^2	0.9897	0.9886	0.7953	0.8611

relationships can be used to verify the tip vortex cavity predictions from the numerical models.

The evaluation is done for single blade passage where the centre frequency of the tip vortex spectral hump is clearly distinguishable. Three advance ratios ($J = 0.4, 0.45, 0.50$) and two cavitation conditions ($\sigma_n = 1.96, 3.10$) are used to generate additional data-points for the proportionality plot. The comparison is shown in Fig. 16, and the regression analysis coefficients are given in Table 3. The proportionality relations pertaining to the mean cavity radius $(\bar{\Upsilon})$, as well as those pertaining to the operating conditions (σ_n, K_T) are checked.

Good linear fits are observed for the four proportionality relations considered, as indicated by high values of the coefficients of determination (R^2). This confirms that the proportionality relationship holds across the range of operating conditions considered. This is particularly the case for proportionality relationships of the hump centre frequency in Figs. 16(a) and 16(b). The linear fit is slightly lesser for the peak source levels. The slope of the best-fit lines in Figs. 16(c) and 16(d) correspond to the empirical constant κ_1 in Eq. (14). In the current work, the numerical method indicates a value of κ_1 in the range of 3.3 to 3.5. This is considered to be similar to the findings in relevant literature (Bosschers, 2018a), where a value of 3 is proposed based on curve-fitting of measured data on a two-bladed research propeller.

An overall good agreement with the proportionality agreements verifies the numerical methods used for the hydrodynamic flow and those used for the acoustics of the tip vortex cavity. The relations pertaining to cavity radius verify the consistency of tip vortex cavity radius output from the ESPPRO hydrodynamic model. The relations pertaining to the operating conditions verify the applicability of the numerical method for the range of propeller operating conditions considered within the current validation study.

5.3.3. Tip vortex cavity geometry

A closer look at the geometry of the tip vortex cavity and its dynamic behaviour is essential to comprehend the adequacy of the piece-wise, curvilinear cylindrical assumption used in the tip vortex cavity numerical models. Fig. 17 shows a visual illustration of the three-dimensional tip vortex cavities downstream of the propeller. The

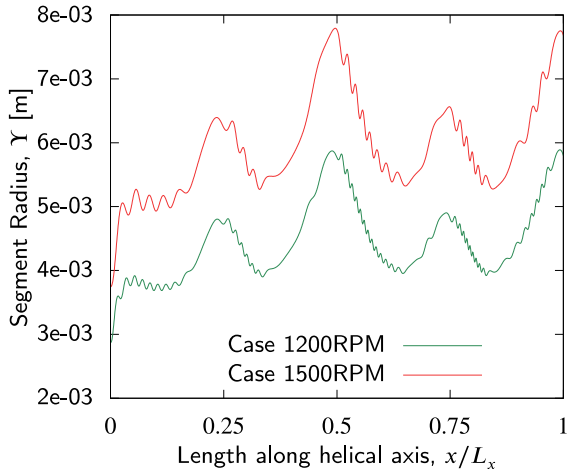

Fig. 18. Instantaneous tip vortex cavity geometry along the helical axis. Origin is at the beginning of the cavity (i.e. at blade trailing edge). The cavity length corresponds to approximately two propeller revolutions.

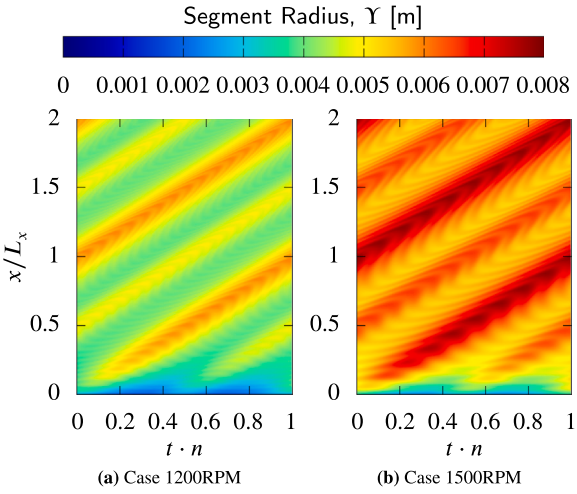

Fig. 19. Spatio-temporal plot of the cavity segment radius. Horizontal axis is non-dimensional time, vertical axis is non-dimensional distance along the helical axis, and the colorbar represents cavity radius.

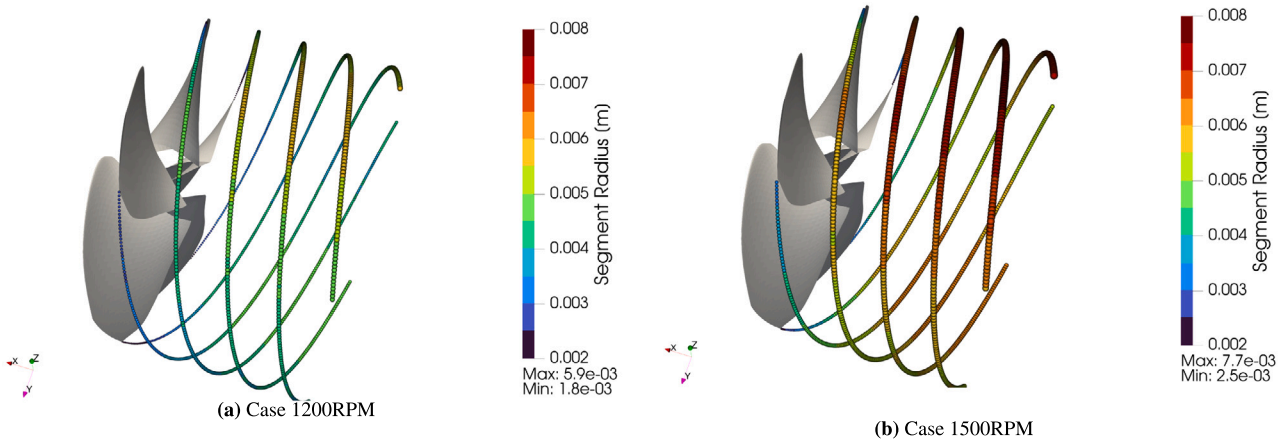

Fig. 17. Instantaneous tip vortex cavity geometry from ESPPRO. Cavity segments are represented as spheres proportional to the segment radius, similar to Model 1D implementation. The cavity length shown in the figure is intentionally truncated for clarity.

corresponding two-dimensional plots along the cavity axis are given in Fig. 18. The influence of the ship wake field is observed through segment radius peaks that correspond to the wake peaks at the 12 o'clock and 6 o'clock positions. The cavity length in Fig. 18 corresponds to the tip vortex cavity generated over two propeller revolutions, hence four such peaks are visible — two major peaks that correspond to cavity segments that were born at the 12 o'clock position and two minor peaks that correspond to segments that were born at the 6 o'clock position (see Fig. 18). The spatio-temporal evolution of the cavity geometry can also be visualized through the contour plot in Fig. 19.

5.4. Uncertainty quantification

While the validation with experimental full-scale measurements provides a practical overview of the acoustic models, it must be noted that this involves a large degree of uncertainty. Uncertainties can be mainly attributed to the measurement setup, the difficulty in simulating various noise sources, and the assumptions used in the numerical model. In order to achieve a sensible comparison of the numerical acoustic predictions with the acoustic measurements, it is necessary to have a rough quantification of these uncertainties.

5.4.1. Uncertainties in the numerical model

Correlating key parameters of the propeller tip vortex cavity to those of a long cylinder (as defined in the verification study in Section 4) shall provide quantitative estimates on the validity of assumptions used in the acoustic models. While the analytical solution is not valid for the propeller tip vortex cavity, the results from the verification study that pertain to numerical resolutions can be reused. This means that relative comparisons can be made between the numerical solution for the finest resolution in the convergence study (Fig. 8) and the solutions corresponding to the resolution used in the propeller validation case. This is also applicable for the results from the sensitivity study on the cavity length (Fig. 10) where the analytical solution is independent of the sensitivity parameter, but not for the other sensitivity parameters.

From the theory of linear waves on cylindrical vortex cavities, it is known that the sound wave frequencies are equal to the wave frequencies on the cavity (Bosschers, 2018a). Thus, the relevant time scales for the simulation of waves on the cavity causing noise emission can be calculated from the relevant multiples of the blade passing frequency $f_{\mathrm{bp}} = n_b n$, where n is the propeller rotation rate and n_b the number of blades. The highest wave frequency requires the smallest time steps for the simulation of the sound radiated from the tip vortex cavity. If the highest frequency to be considered is the hth harmonic of the blade passage frequency, hf_{bp}, the number of time steps per period is

$$n_t = \frac{2\pi}{\Delta\psi}\frac{n}{hf_{\mathrm{bp}}} = \frac{2\pi}{\Delta\psi}\frac{1}{hn_b}. \tag{15}$$

The number of time steps per period (n_t) for the first to sixth harmonics, with 0.5° propeller rotation per time step, are 144, 72, 48, 36, 28.8, and 24, respectively.

The axial resolution can be calculated using an appropriate relation between the cavity surface wavelength and wave frequency. While theoretical estimates of dispersion for cavity dynamics are available (Bosschers, 2018a), they may not be valid for the current setup because the cavity segments in the numerical flow model are treated independent from each other. Thus, as mentioned by Gosda et al. (2021), there is no axial propagation of waves other than with the ambient velocity, the pulsating segments are swept downstream with. However, a dispersion relation for the numerical method can be obtained by performing a spatio-temporal Fourier transform of the cavity radius, as seen in Fig. 20. The frequency and wave-number axes are normalized by appropriate quantities to showcase the inter-dependency of the surface waves along the cavity surface and their frequency, i.e. the dispersion relation. The two-dimensional Fourier transform shows three distinct bands where the cavity fluctuations are dominant.

The central band shows the influence of the blade loading on cavity radius fluctuations. The helical length traversed by the cavity surface wave during one propeller revolution ($L_{1\mathrm{rev}} = L_x/2$) is linked to the cavity surface fluctuations at the propeller rotation frequency. This is referred to as 'helical wavelength' in subsequent discussion. The hth harmonic wave is linked to a wavelength that is $1/h$ of the helical wavelength. This is indicated by the central band, which is essentially a straight line that has a slope of −1.

The side-bands indicate dominant cavity radius fluctuations for surface waves that have a much higher wave number (i.e. much smaller wavelength) than the surface waves generated due to blade loading. These are the radius fluctuations induced by cavity dynamics, and the corresponding dispersion relation is indicated by the red dotted-line. These are the shortest-wavelength waves that are relevant to acoustic computations. It can be seen from Fig. 20 that the shortest wavelength required to be captured, for accurate prediction up to the sixth harmonic of propeller rotation frequency (vertical axis), is approximately 1/25th the helical wavelength for case 1200RPM; and approximately 1/20th the helical wavelength for case 1500RPM. The limiting value of wavelength from the numerical dispersion relation is used to define the axial resolution of the numerical model. As the numerical model discretization is such that a cavity segment is created

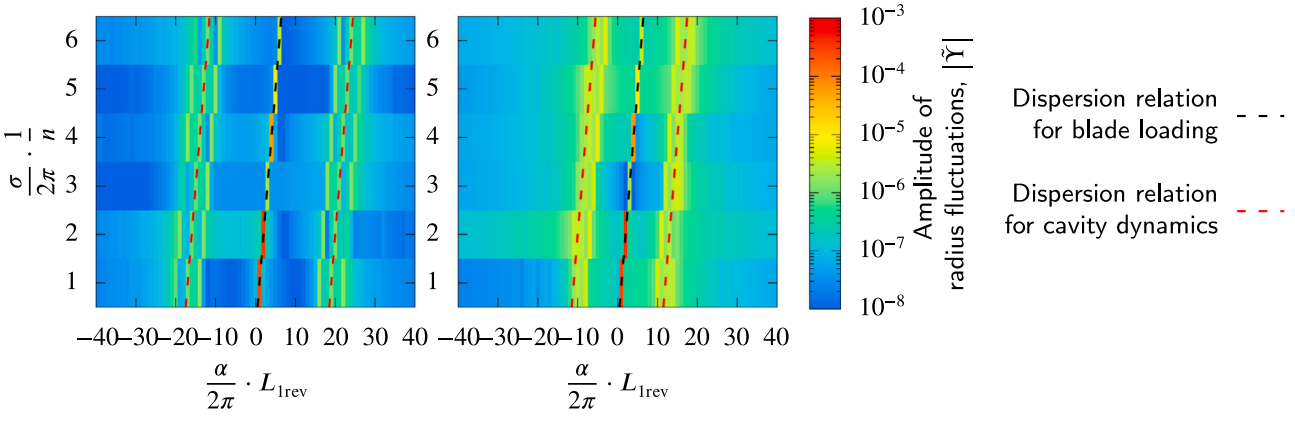

(a) Case 1200RPM **(b)** Case 1500RPM

Fig. 20. Spatio-temporal discrete Fourier transform of the cavity segment radius from a single blade. Only the second spatial wavelength of the cavity radius along the helical axis is included (i.e. $x/L_x > 0.5$) so as to ensure periodicity. The horizontal axis is the non-dimensional frequency, normalized by the propeller rotation frequency. The vertical axis is the non-dimensional wave number, normalized by the helical cavity length generated from 1 propeller rotation (i.e. $L_{1\mathrm{rev}} = L_x/2$).

for every 0.5° of propeller revolution, approximately 28.8 segments are present per the smallest wavelength required to be captured.

The temporal and spatial resolution of the propeller tip vortex cavity can be examined in conjunction with the verification study in Section 4.2. Assuming that the numerical convergence study remains valid for the propeller tip vortex cavity, the numerical resolution errors for the validation study can be extracted. For the range of blade harmonics considered, the maximum error for model 1D is approximately 3% and that for model 2D is approximately 1%. An additional error is introduced due to the length of the tip vortex cavity considered. Due to computational restrictions, the numerical model only uses a cavity length that is approximately twice the largest wavelength. From the sensitivity plot in Fig. 10, this leads to an approximate error of 10% including 1% resolution error. Combining the errors due to spatial, temporal and cavity length resolutions give an error of approximately 1 dB for Model 1D and 0.8 dB for Model 2D.

While the error from the acoustic models for tip vortex cavitation is estimated from the above procedure, similar quantitative estimates are not known for the flow simulations in ESPPRO and for the acoustic models of blade displacement noise and sheet cavitation noise. However, the focus of the current paper is on the numerical models related to tip vortex cavitation acoustic, hence only these uncertainties are included.

5.4.2. Measurement uncertainties

The source levels presented in Humphrey et al. (2015) are subject to uncertainties introduced by the source conditions, quality of measurements and processing techniques. The variability in the ship's acoustic source condition affects the repeatability and reproducibility of the measurements. The quality aspect of measurements is related to the sensitivity and calibration of the hydrophones, amplifiers and other related instrumentation required to realize the acoustic measurements. Further uncertainties are introduced in the processing of time domain signals to frequency domain spectra. These are a few of the aspects (ISO17208-1, 2016) that need to be considered if a rigorous measurement uncertainty estimate is to be evaluated. Such an extensive evaluation is not envisaged for the current validation study. Nevertheless, approximate estimates are extracted from the literature, as follows.

Uncertainty estimates:. Humphrey et al. (2015) quantify the variability of the experimental setup, by analysing the measurement data. The analysis estimates the variability between different runs of the vessel to be of the order 1 to 2 dB. The random systematic variability that might be expected for measurements using multiple hydrophone arrays have been summarized as a function of one-third octave band frequency in Figure 18 of Humphrey et al. (2015). This amounts to about ±2.5 dB in the range of the first blade harmonic and reduces to about ±1 dB for the highest frequencies considered in the current comparison (about 500 Hz). A further uncertainty of ±2 dB is considered for the uncertainty in the source characterization through source level corrections, as suggested in Section 5 of ISO17208-2 (2019). These values have been used to define a 'measurement uncertainty band' for the current validation study.

Concurrent noise sources:. The measured noise levels include the contributions from other noise sources such as the ship engine, shaft rotation, waves, flow turbulence etc. These contributions are not considered in the current validation study because the numerical acoustic predictions are only expected to be reliable for multiples of the blade passing frequency (f_{bp}). For the five-bladed Princess Royal propeller, the first harmonic of the shaft rate is equivalent to $0.2f_{bp}$. Therefore, the shaft harmonics are not expected to have significant bearing on the acoustic spectrum in the frequency range where tip vortex cavitation-induced noise is expected to be dominant (i.e. $f > 2f_{bp}$). Similar considerations for the engine harmonics also indicate an unlikelihood of interaction between engine and blade harmonic noise levels. The Princess Royal vessel is equipped with a gearbox with reduction ratio of 1.75, which means that the first engine harmonic is approximately equal to $0.35f_{bp}$. Hence it is reasonable to assume that the blade harmonics up to the 7th harmonic are not influenced by the machinery-induced noise. A further comprehensive analysis of the machinery-induced noise from the full-scale noise measurements can be found in Turkmen et al. (2017a). Stochastic processes such as water waves and flow turbulence are expected to induce noise signals that are predominantly of broadband nature. As the current comparison only involves tonals, these contributions are also disregarded.

Background noise:. Background noise refers to other noise sources in the sea environment where the noise measurements take place. These are corrected for during the processing of the measurement results. The accuracy of this methodology is unknown, and hence no uncertainty on this aspect is further highlight to the experimental measurements. It is not expected to have background noise sources whose frequencies coincide with the blade passing frequency.

5.4.3. Uncertainties in recreating the measurement scenario

The experimental measurement scenario is defined by the noise from a twin-screw catamaran vessel, with propellers operating at approximately 1.2 m below the water surface, and a sea bottom of approximately 100 m depth. However, the numerical simulation scenario is defined by the noise produced from a single propeller, rotating in a non-uniform ship wake field, which includes acoustic models for radiated noise from the rotating blades, the sheet cavities and the tip vortex cavities. A schematic comparison of the measurement and simulation scenarios is shown in Fig. 21. A realistic numerical prediction should be able to account for the additional noise sources in the experimental

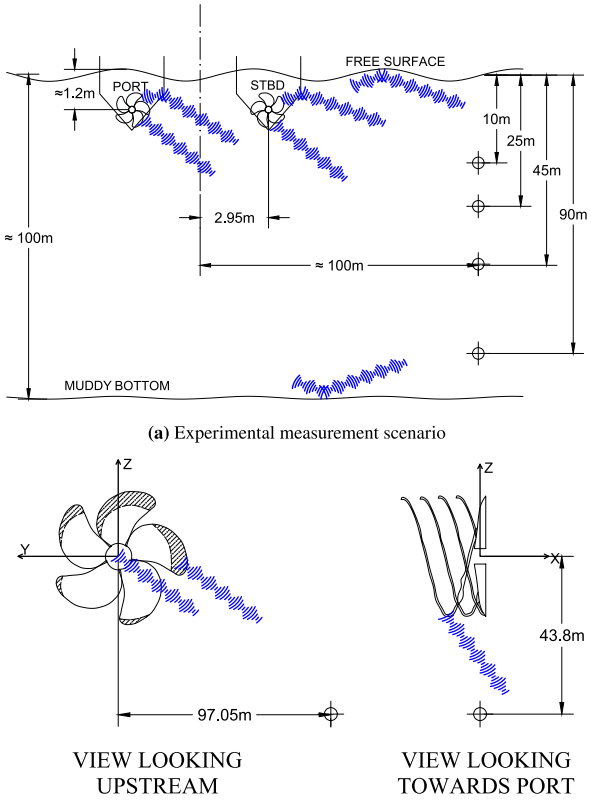

(a) Experimental measurement scenario

(b) Numerical simulation scenario

Fig. 21. Schematic comparison of the measurement setup and the numerical simulation setup. Blue lines are symbolic representation of acoustic waves and their reflection paths included in each scenario, indicating noise mechanisms.

measurement scenario. The following itemized points provide a description of the additional noise sources, their associated uncertainties, and how they amplify/reduce the numerically predicted noise. The higher uncertainty bound is a quantification of the situation which produces maximum amplification of the numerically predicted noise, and vice versa.

Free surface reflection:. The air–water interface acts as a reflecting boundary resulting in the typical Lloyd-mirror interference pattern (LMIP) (de Jong, 2009). Due to the relatively lower acoustic impedance of air, the reflection coefficient of the interface is close to −1, thereby resulting in a reflected signal that is almost 180° out-of-phase with the original source signal. The theoretical reduction in source levels due to LMIP can be calculated by using an 'image interference effect' for a source near an out-of-phase reflecting surface (Carey, 2009). The resultant correction (ΔSL_{LMIP}) is given by:

$$\Delta SL_{LMIP} = 10\log_{10}\left(4\sin^2\left(\frac{kz_s z_r}{r_{sr}}\right)\right), \tag{16}$$

where k is the wavenumber, z_s and z_r are source and receiver depths respectively, and r_{sr} is the source–receiver range.

The correction for free surface reflection is estimated based on Eq. (16) for the 45 m deep hydrophone. The interference patterns in the real sea are not as clearly defined as in the LMIP; nonetheless, it provides a quantitative estimate of the limits of uncertainty due to free surface reflection. It may also be noted that the interference effects are much higher for lower frequencies, and consequently also the sensitivity of the noise measurement data for lower frequencies. Inaccuracies in Eq. (16) are estimated by considering ±10% error in the argument of the sine function. This defines the upper and lower bounds of uncertainty due to free surface reflections.

Sea bottom reflection:. The test site for the experimental measurements has an approximate depth of 100 m, which is classified as shallow water as per the ISO-17208 guidelines (ISO17208-2, 2019). Accordingly, significant amplification of the noise, due to reflected sound from the sea bottom is expected. The difficulty of estimating source levels in shallow water is investigated in MacGillivray et al. (2023), which includes a semi-empirical estimate of an adjusted source level. This is based on a consideration of an effective dipole sound field consisting of the point source and its reflected image by the sea surface. The increase in source levels due to seabed reflections is given by:

$$\Delta SL_{Btm} = 10\log_{10}\left(\check{R}_{btm}\frac{14(kz_s)^2 + 2(kz_s)^4}{14 + 2(kz_s)^2 + (kz_s)^4}\right). \tag{17}$$

Here, the argument of the log-function is multiplied by a correction factor proportional to the reflection coefficient of the sea bottom ($\check{R}_{btm}$). This is assumed to be equal to 0.38, based on the geo-acoustic parameters given in the literature for the same test site (Turkmen et al., 2017b). Similar to the uncertainty estimate for free surface reflection, ±10% error on the wave number is considered to estimate the uncertainty range for sea bottom reflection.

Hull and appendages:. It is impractical to include a three-dimensional model of the ship hull and appendages to account for reflection effects in the acoustic simulations. In conformance with usual practice for ship acoustic simulations, a solid boundary factor (SBF) is applied in order to account for these effects. The theoretical maximum limit of SBF is 2.0, which corresponds to doubling of the propeller acoustic signal, similar to reflection from hard, flat plate. The lower limit considered is the case where the hull reflections have no effect, i.e. SBF = 1.0. Accordingly, the upper and lower bounds of uncertainties due to hull reflection are 0 dB and −6 dB respectively.

Second propeller:. The experimental measurements were performed while both propellers on the vessel were in operation, while the simulations are performed for a single propeller. As a simple estimate of the increase in source levels due to the second propeller, the same acoustic source can be reflected about the ship centre-line to obtain a reasonably accurate estimate of the resultant sound field. The theoretical maximum increase due to the second propeller is 6 dB, which corresponds to doubling of the source levels. The minimum limit is taken as 0 dB. It may be noted that numerical simulations estimate a possibly wider range of uncertainties depending on the synchronization between the propellers (Scharf et al., 2024). Such wider range of uncertainties is not considered in the current paper due to lack of available information about shaft synchronization.

Source and receiver locations:. The narrowband spectra used for validation are that of the measured acoustic pressure levels at a particular hydrophone location. Therefore, the measurements are sensitive to any inaccuracy in determining the exact source and/or receiver locations. The coordinates of the source and receiver locations in the experimental measurements are only nominal. In practice, it is difficult to ensure the exact locations during a sea trial, unlike in model scale testing. An approximate 10% error is considered in the distance (the same as for free surface reflection uncertainties), and the upper and lower bound of error considered on the basis of a spherical spreading approximation.

Smearing effect:. The numerical predictions assume a perfectly periodic acoustic pressure signal, as the propeller rotation speed is prescribed to a constant value and the wake field is assumed to be time-invariant. Such an assumption of periodicity results in distinct peaks at the tonals, as seen from the dashed lines in Fig. 15. However, the full-scale measurement condition is subject to non-periodic inflow variations or turbulence, resulting in the acoustic power at the tonals being spread over a small band of frequencies. This is known as the 'smearing effect' on the tonal components in the spectrum (van Wijngaarden et al., 2005). Consequently, the experimentally measured noise levels are lower than the numerically predicted levels, because the tonal acoustic energy in the latter are concentrated on a single frequency. A correction for this overprediction is made by estimating the frequency band over which the smearing occurs (Δf_{smear}) for each blade harmonic, and for each operating condition. Thereafter, the correction to the numerical predictions is given by:

$$\Delta SL_{smear} = -10\log_{10}\left(\frac{1}{\Delta f_{smear}}\right). \tag{18}$$

The resulting correction ranges from around 3 to 6 dB across different harmonics.

5.4.4. Consolidated uncertainties

A summary of the quantified uncertainties is provided in Table 4. The uncertainties in reported source levels are used to indicate a confidence interval within which the experimentally measured source levels from Brooker and Humphrey (2016) are expected to be reliable. The uncertainties in numerical characterization are highlight to the numerically estimated source levels, in order to achieve a reasonably realistic estimate of the full-scale measurement scenario. It may be noted that the uncertainty estimates in Table 4 are only indicative estimates, and are not entirely based on mathematically justifiable uncertainty calculations. The purpose of such an estimate is to highlight the fidelity of the validation process while comparing with full-scale measurements.

5.5. Results and qualitative comparison

After accounting for the various uncertainties between the experimental and numerical simulation scenarios, the power spectral density levels are compared in Fig. 22. The 1 Hz narrowband source level spectrum from Humphrey et al. (2015) is normalized with the blade passing

Table 4
Summary of minimum and maximum levels of uncertainty in source levels. All tabular values are calculated in dB, re 1 μPa^{2}m^2. Uncertainty ranges for free-surface and bottom reflection are frequency dependent, where k is the associated wave number.

Uncertainty parameter	Minimum	Maximum
Uncertainties in reported source levels		
(1) Measurement repeatability	−2	+2
(2) Measurement setup	−1 to −2.5	+1 to +2.5
(3) Source level corrections	−2	+2
Uncertainties in numerical characterization		
(1) Free-surface reflection (according to Eq. (16))	$-\Delta SL_{LMIP}(0.9k)$ for $z_r = 43.8$ m, $r_{sr} = 97.05$ m	$-\Delta SL_{LMIP}(1.1k)$ for $z_r = 43.8$ m, $r_{sr} = 97.05$ m
(2) Bottom reflection (see Eq. (17))	$\Delta SL_{Btm}(1.1k)$	$\Delta SL_{Btm}(0.9k)$
(3) Hull and appendages	0	+6
(4) Second propeller	0	+6
(5) Source & receiver locations	$20\log_{10}(0.9)$	$20\log_{10}(1.1)$
(6) Smearing effect (see Eq. (18))	ΔSL_{smear}	0
Uncertainties due to numerical resolution		
(1) Model 1D	−1.0	+1.0
(2) Model 2D	−0.8	+0.8

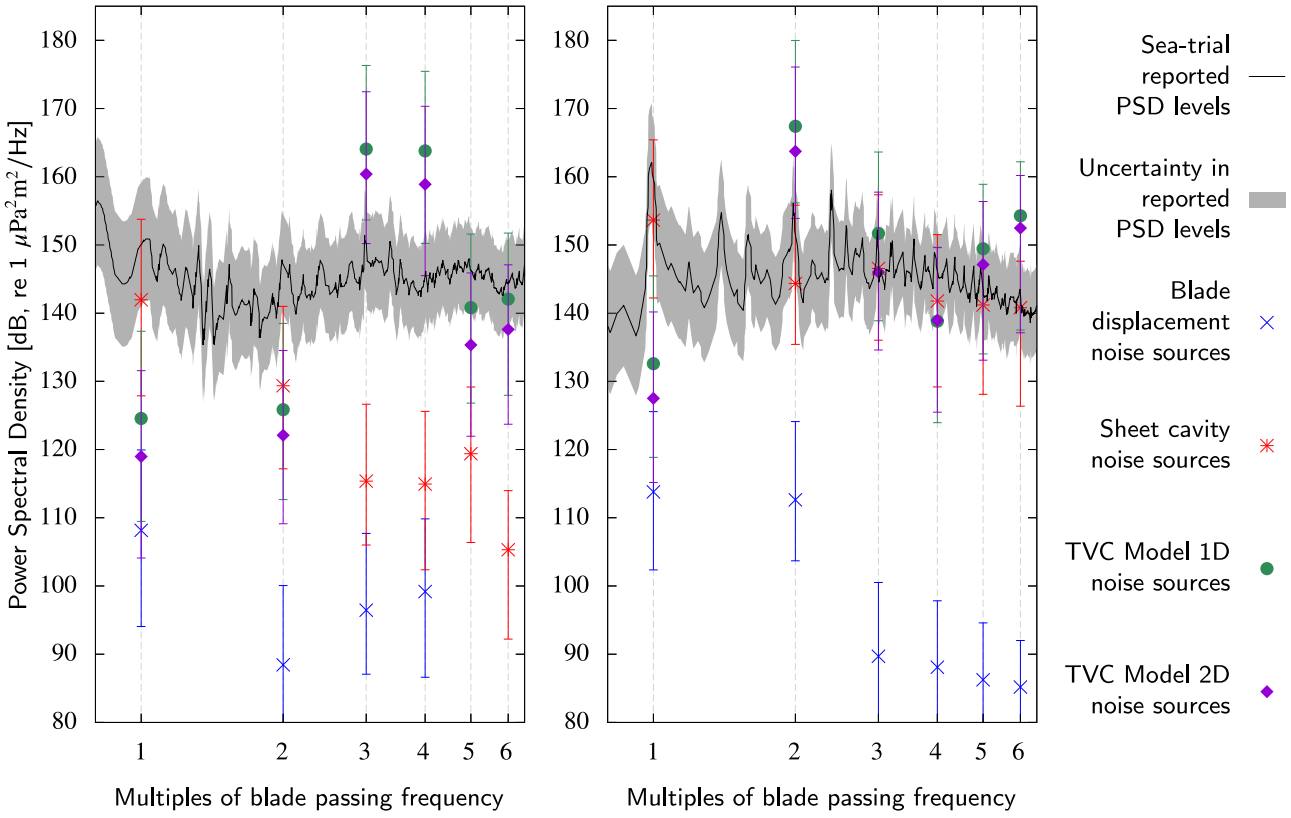

(a) 1200RPM case **(b)** 1500RPM case

Fig. 22. Comparison of numerically predicted power spectral density levels with experimentally reported levels, in 1 Hz bandwidth. Uncertainty in sea-trial reported source levels and error-bars for numerically predicted noise sources are calculated in accordance with Table 4.

frequency for each case. The uncertainties in the sea-trial reported source values are indicated with a grey band around the source level spectrum. The numerical simulation results are indicated by markers, showing the predictions at blade harmonics. The numerical prediction of source levels are calculated as follows: The amplitude of pressure fluctuations ($\hat{p}$) at the hydrophone location (x=0 m, y=−97.05 m, z=−43.8 m, r=106.48 m) is normalized to 1 m radial distance from the propeller centre. The root-mean-square value of the resultant power spectrum is converted to the deciBel scale with a reference power of 1 μPa^{2}m^2 to obtain the source levels (SL). Since the numerical prediction method only includes tonal noise, the power spectral density levels (PSDL) in 1 Hz bandwidth are the same as the source levels. Eq. (19) summarizes the procedure.

$$\mathrm{PSDL} = 20log_{10}\left(\frac{\tilde{p}/\sqrt{2}}{1\times10^{-6}}\right) + 20log_{10}(r) \tag{19}$$

In the potential flow based numerical simulations, one is able to separate the acoustic contribution from different acoustic sources. This is helpful in highlighting the dominant propeller noise mechanisms for different harmonics. For example, it is evident from the different acoustic source contributions that the blade displacement induced tonal noise is dominated by the cavitation-induced tonal noise. This is expected for the two operating conditions considered here, wherein considerable cavitation is present. Blade displacement induced tonal noise is relevant

for non-cavitating operating conditions. However, such conditions are not presented in this paper, due to the low signal-to-noise ratio of the experimental measurements.

The tonals at lower harmonics are dominated by the sheet cavity-induced noise. The numerically predicted source levels at the first harmonic can be almost entirely attributed to sheet cavitation. These levels, after accounting for the uncertainties in the numerical characterization, fall within the uncertainty range of the reported power spectral density (PSD) levels from the sea-trials. The contribution of the tip vortex cavity induced noise becomes prominent at higher harmonics, as is evidenced by the frequency hump in the sea-trial PSD levels. A visual estimate places the centre frequency of the tip vortex spectral hump to be between the third and fourth blade harmonics for the 1200RPM case, and between the second and third harmonics for the 1500RPM case. The numerical predictions also indicate similar ranges of dominant tip vortex induced noise frequencies. These estimates are also in line with the empirical estimates based on cavitation number and thrust coefficient (Bosschers, 2018a; Berger, 2018). It may be reiterated here that the tuning of the tip vortex model is done only based on the 1200RPM operating condition; the same parameter settings are used for the 1500RPM operating condition. A reasonably accurate prediction of the tip vortex frequency hump points towards the applicability of the acoustic models for propeller tip vortex cavitation noise estimation.

The cumulative harmonic value is not indicated to manage the readability of the plots, but the uppermost marker on each vertical line can be treated as the cumulative value. Since the uppermost value is generally significantly larger than the next, the difference on the deci-Bel scale is negligible. As can be seen from the comparison in Fig. 22, the numerical prediction provides a decent estimate of the full-scale noise source levels, within the range of uncertainties discussed earlier. Since the uncertainty range is non-negligible, the primary emphasis of the comparison is not on the accuracy of the predictions, but on the qualitative prediction of the source levels. The numerical predictions concur with the general expected trend of relatively higher noise levels at lower harmonics (first and second) for the 1500RPM case. For harmonics from third to sixth, the source levels for the 1200RPM case are at similar levels to the 1500RPM case. This trend is also qualitatively predicted from the numerical simulations. There seems to be a slight misalignment in the source levels close to the tip vortex spectral centre frequency, i.e. between the third and fourth harmonic. This can be attributed to the current lack of an established procedure for tuning the tip vortex cavitation flow model. The availability of validation data for more operating conditions and a better understanding of the influence of the tuning parameters can further streamline the tuning process, thereby enabling better predictions.

The comparison between the tip vortex acoustic models – Model 1D and Model 2D – shows good agreement across all harmonics. Both models show consistent predictions for the tip vortex 'frequency hump' — between 3rd and 5th harmonics for the 1200RPM case, and between 2nd and 3rd harmonics for the 1500RPM case. The relation between adjacent harmonics is also consistent between the models. A maximum difference of 8 dB is seen for certain harmonics, which points towards the possible error due to the simplifications in Model 1D. Such relative error is acceptable considering the higher range of uncertainties from other sources. The time domain comparison between the acoustic pressure signals predicted at the hydrophone location from both models is shown in Fig. 23, indicating good overall agreement between the signal amplitudes. The phase of the signals is also well aligned, except for a slight shift in the 1500RPM case. This is possibly because the directional effects accounted for by Model 2D are more pronounced for large amplitude cavity fluctuations. The shift in phase does not affect the noise amplitude prediction, and hence is not investigated further.

It is promising that the cumulative noise harmonics from the simulation lies within the expected range of uncertainties for the validation exercise. However, it is unfortunate that such high levels of uncertainty make it difficult to conclude about the overall accuracy of the simulation setup. It is also difficult to ascertain whether the models under-predict or over-predict the measurements, due to the various uncertainty parameters discussed earlier. Nevertheless, considering the complexity of the noise simulation problem and the low fidelity of the numerical models, a decent agreement is obtained for the validation study cases. A qualitative comparison of the tip vortex models also points towards their applicability for propeller tip vortex cavitation problems.

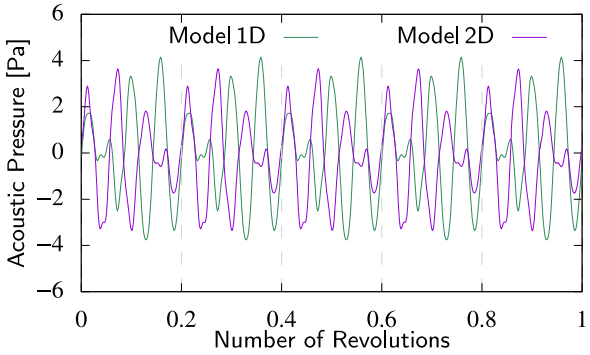

(a) 1200RPM case

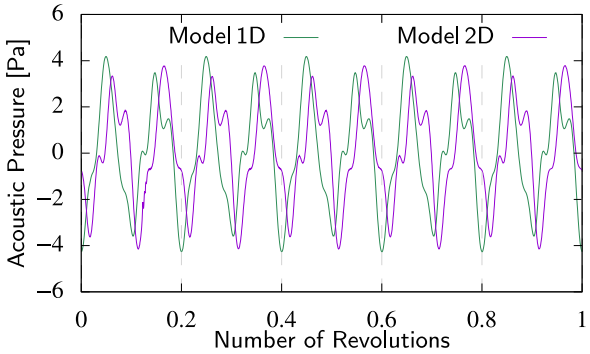

(b) 1500RPM case

Fig. 23. Simulated acoustic pressure signals at the 45 m deep hydrophone.

Further enhancement of the accuracy of the numerical predictions is directly related to reducing the uncertainty ranges mentioned in Table 4. From the numerical simulation standpoint, this means improved source models that are able to better represent the ocean environment reflections and the broadband noise spectrum. Characterization of the sea-trial ocean environment is computationally cost-intensive, and the use of low-fidelity reflection models is perhaps better suited for the current numerical prediction scenario. The broadband characteristics of the noise spectrum is mainly inherited from the flow solver for acoustic analogy problems. Their inclusion requires flow solvers that can account for the stochastic fluctuations of the cavity surfaces. Alternatively, post-processing semi-empirical models for tip vortex cavity broadband noise, such as the one proposed in Bosschers (2018b), present potential avenues for consideration.

6. Conclusion

The importance, practicality, implementation and validation of numerical models to predict the acoustic radiation from propeller cavitation are discussed in this paper. The importance of developing numerical acoustic models for tip vortex cavitation is highlighted by the extremely high grid resolution required to simulate the same using high-fidelity Navier–Stokes equation solvers. Most practical applications related to propeller underwater noise cannot handle such high computational costs. The low-fidelity acoustic models proposed and

implemented in this paper point towards the practicality and cost-efficiency for such applications. As is the case for all low-fidelity models, it is important to characterize the compromise in accuracy achieved by simplifying the numerical models. The verification and validation exercises performed within the paper are aimed towards this end. The acoustic pressure predicted by both numerical models are in good agreement with the analytical solution for the verification case study, within the limitations of the assumptions.

The validation case study aims to assess the practical utility of the acoustic models. The limitations of the validation case have been explored with an attempt to characterize and quantify the range of uncertainties. While the uncertainty evaluation is by no means complete, it provides an indication about the expected deviations when validating against full-scale noise measurements. A conclusive claim about the validity of the numerical models cannot be made with this evaluation; but the predictions from the numerical models are found to be in decent agreement for the validation cases considered.

The validation study could be enhanced by including additional operating conditions, especially conditions with significant tip vortex cavitation but no sheet cavitation. However, the experimental measurements are unreliable for such cases, with low signal-to-noise ratio. Despite very strong reflection effects, cavitation tunnel measurements can provide a further possibility for validation. This is earmarked as follow-up studies for the current numerical acoustic models.

The simplicity of the numerical acoustic models allows rapid coupling to any hydrodynamic flow model that simulates tip vortex cavity dynamics. An example implementation is performed within the scope of the current work, where the models are coupled to a propeller potential flow solver. The successful implementation paves the way to future investigations and evaluation studies which would enhance the applicability of the numerical models. Any improvement in the flow characterization of the hydrodynamic model directly improves the accuracy of the acoustic model. It would be important to consider higher-order hydrodynamic models for the tip vortex rather than the piece-wise cylindrical representation currently implemented in ESPPRO .

One major limitation observed while coupling the proposed numerical models to a potential flow solver is the inability to predict the broadband nature of the tip vortex noise spectrum. The current methodology assumes periodic behaviour of tip vortex cavity fluctuations; whereas in reality, the behaviour is affected by the random, turbulent nature of the surrounding flow. Even though the dominant frequency range can be approximately predicted by the current methodology, a more reliable estimate would require the inclusion of the broadband noise spectrum. The work conducted by Bosschers (Bosschers, 2018a), based on random phase and amplitude modulation, is a promising endeavour for subsequent research.

Within the limitations posed by the complexities of the underwater noise phenomenon, the current study takes a major stride towards the development of low-fidelity numerical acoustic models for tip vortex cavitation induced noise. Relevant analytical and practical cases have been evaluated, ascertaining the applicability of these methods. Enhancing the quality of the input flow to the model, such as the inclusion of the broadband nature of the cavity fluctuations and improved tip vortex cavity dynamics, would serve as upgrades to the current numerical acoustic models. In this respect, the results obtained in the current study lay the groundwork for further development of the acoustic models. Further exploration is intended in this direction, enabling extensive application of the low-fidelity numerical models for propeller tip vortex cavity acoustics.

CRediT authorship contribution statement

Joseph Praful Tomy: Writing – original draft, Visualization, Validation, Software, Methodology, Investigation, Formal analysis, Data curation, Conceptualization. **Roland Gosda:** Writing – review & editing, Visualization, Validation, Software, Methodology, Investigation, Formal analysis, Data curation, Conceptualization. **Stephan Berger:** Writing – review & editing, Visualization, Validation, Supervision, Funding acquisition, Conceptualization. **Harry B. Bingham:** Writing – review & editing, Supervision, Funding acquisition. **Poul Andersen:** Writing – review & editing, Supervision, Funding acquisition. **Moustafa Abdel-Maksoud:** Writing – review & editing, Supervision, Project administration, Funding acquisition, Conceptualization.

Declaration of competing interest

The authors declare the following financial interests/personal relationships which may be considered as potential competing interests: Joseph Praful Tomy reports financial support was provided by Innovation Fund Denmark and MAN Energy Solutions. Roland Gosda reports financial support was provided by Federal Ministry for Economic Affairs and Climate Action (BMWK) and Projektträger Jülich (PtJ). Stephan Berger reports financial support was provided by MAN Energy Solutions and FORCE Technology. Other authors declare that they have no known competing financial interests or personal relationships that could have appeared to influence the work reported in this paper.

Data availability

Data will be made available on request.

Acknowledgements

The authors would like to thank Innovation Fund Denmark for financially supporting the research project [grant number 0153-00080B]; the Federal Ministry for Economic Affairs and Climate Action (BMWK) and Projektträger Jülich (PtJ) for the funding of the work through ProptiFo [grant number 03SX516F], part of the research project DEff-ProForm; MAN Energy Solutions for financial and resource support; Kaushik Ravi for the preliminary investigations of Model 2D with surface-based discretization for a pulsating sphere; Martin Scharf and Keun Woo Shin for technical discussions that aided the research work.

Appendix A. Approximation of the surface area

In this section the calculation of the partitioned surface area of a harmonic wave as used in this article is investigated. The analytical solution is compared with approximations from (20) and (21) based on cylindrical and conical sections.

$$A \approx 2\pi\Upsilon\left(\frac{x_0+x_1}{2}\right)(x_1-x_0) \tag{20}$$

$$A \approx \pi(\Upsilon(x_1)-\Upsilon(x_0)) \sqrt{(\Upsilon(x_1)-\Upsilon(x_1))^2+(x_1-x_2)^2} \tag{21}$$

It will be shown, that the approximations converge with second order.

To measure the error of the approximations, the analytical area of a partition of the oscillating, cavitating cylinder defined on $x \in [x_0, x_1] \times \theta \in [\theta_0, \theta_1]$ can be calculated using

$$\begin{aligned} A &= \int_{x_0}^{x_1}\int_{\theta_0}^{\theta_1} \Upsilon\sqrt{1+\left(\frac{\partial\Upsilon}{\partial x}\right)^2}\,d\theta dx \\ &= (\theta_1-\theta_0)\int_{x_0}^{x_1}(a+b\cos(\alpha x-\sigma t)) \\ &\qquad \sqrt{1+(-\alpha b\sin(\alpha x-\sigma t))^2}\,dx. \end{aligned} \tag{22}$$

See e.g. Bronshtein et al. (2015, p.502) for the calculation of the curve length of a function. For convenience $s = \alpha x - \sigma t$ is introduced.

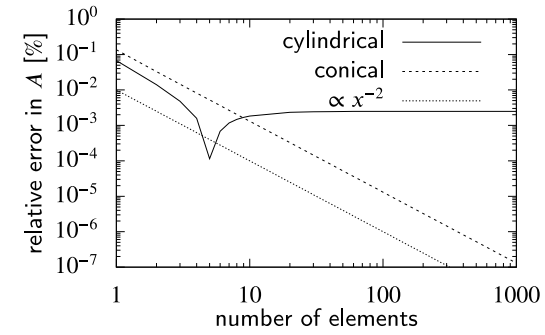

(a) Relative error of the approximate area.

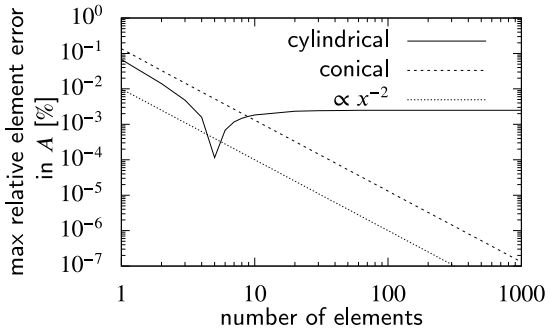

(b) Maximum relative error of the approximate area per element.

Fig. 24. Relative and maximum error of the area approximations.

Integration by substitution (Bronshtein et al., 2015, p.484) then leads to

$$A = \frac{\theta_1 - \theta_0}{\alpha} \int_{s(x_0)}^{s(x_1)} (a + b\cos(s)) \sqrt{1 + (-\alpha b \sin(s))^2}\, ds. \tag{23}$$

The integral may be split into

$$\begin{aligned} &\int_{s(x_0)}^{s(x_1)} a\sqrt{1 + (-\alpha b \sin(s))^2}\, ds \\ &= a\left(\mathcal{E}(s(x_1), i\alpha b) - \mathcal{E}(s(x_0), i\alpha b)\right), \end{aligned} \tag{24}$$

where $\mathcal{E}(\varphi, k) = \int_0^{\varphi} \sqrt{1 - k^2 \sin^2(\vartheta)}\, d\vartheta$ is the elliptic integral of the second kind (Byrd and Friedman, 1971), and

$$\begin{aligned} &\int_{s(x_0)}^{s(x_1)} b\cos(s)\sqrt{1 + (-\alpha b \sin(s))^2}\, ds \\ &= \int_{u(s(x_0))}^{u(s(x_1))} \frac{\partial u}{\cancel{\partial s}} \frac{\cancel{\partial s}}{\partial u} \sqrt{1 + u^2}\, \partial u \\ &= \frac{1}{2}\left(u\sqrt{1 + u^2} + \operatorname{arsinh} u\right)\Big|_{u(s(x_0))}^{u(s(x_1))}, \end{aligned} \tag{25}$$

with $u = \alpha b \sin(s)$. See e.g. Merziger et al. (2010) for the general solution of integrals of the form $\int \sqrt{a^2 + x^2}$.

Figs. 24(a) and 24(b) show that the error both globally as well as the maximum error per element converges with second order for the number of elements per wavelength. While the error of the cylindrical approximation stagnates around $5 \cdot 10^{-3}$%, the conical approximation shows no stagnation for up to 1000 elements.

As shown in Figs. 8(a) and 8(b) the methods introduced in this article converge with the same order. The absolute error accepted for the acoustic amplitude in the models, that use the cylindrical approximation, is around 1%. The stagnation of the error for the cylindrical approximation of the area is two magnitudes lower. Thus, since the area is a multiplicative term in (7), the error of the approximation is expected to have negligible influence on the overall error.

Appendix B. Potential theory-based model for the propeller flow, including effects of sheet cavitation

ESPPRO has been developed at DTU (Technical University of Denmark) in order to solve the unsteady potential flow problem for cavitating marine propellers. The flow problem is formulated using a Cartesian coordinate system rotating with the propeller (see Fig. 21(b)). The total velocity field $\boldsymbol{U}_{\text{total}}$ is understood as a superposition of the undisturbed onset velocity field $\boldsymbol{U}_{\infty}$ due to a prescribed wake field as well as the rotation of the propeller and the induced velocity field $\boldsymbol{U}_{\text{induced}}$, which is assumed to be irrotational, inviscid and incompressible. Under these assumptions it is possible to find a potential Φ for the induced velocity field such that $\boldsymbol{U}_{\text{total}} = \boldsymbol{U}_{\infty} + \nabla\Phi$, where the potential Φ fulfils Laplace's equation $\nabla^2\Phi = 0$.

ESPPRO follows the classical approach for panel codes based on Green's identity, where a surface distribution of sources and dipoles as elementary solutions of Laplace's equation is applied in order to describe the potential of the induced velocity field. In particular, sources σ and dipoles μ are placed on the blade surface S_B and cavitating portions of the trailing wake S_{CW}, whereas only dipoles are placed on the wetted part of the trailing wake $S_W \setminus S_{CW}$.

To obtain a physically meaningful flow field, sources and dipoles are found such that a number of boundary conditions are fulfilled:

- The flow normal to the wetted blade surface $S_B \setminus S_{CB}$ vanishes, i.e. $\boldsymbol{U}_{\text{total}} \cdot \hat{\boldsymbol{n}} = 0$ where $\hat{\boldsymbol{n}}$ is the surface normal vector.
- At the trailing edge of the blade, the Kutta condition $\Delta p = 0$ holds, meaning that the pressure jump $\Delta p = p_l - p_u$ between upper and lower side of trailing edge vanishes. This boundary condition can be linearized yielding Morino's Kutta condition $\Delta\mu_W = \mu_l - \mu_u$ defining the relation between the dipole strengths of the upper and lower side of the trailing edge and the dipole strength of the wake surface directly behind the trailing edge.
- The pressure on cavitating parts of the blade S_{CB} and the trailing wake S_{CW} is constant and equals the vapour pressure p_v, i.e. $p = p_v$.
- The cavity surface, i.e. the interface between vapour and water is regarded as an impermeable surface. This means that there is no flow through the cavity surface on S_{CB} and S_{CW}.

In order to obtain a solution numerically, the boundaries are discretized by quadrilateral panels and constant dipole and source strengths over one panel are assumed. For non-cavitating flow, applying the first two boundary conditions to the discretized problem, a system of linear equations can be set up which can easily solved by the Gauss method. In order to reduce the computational effort, the shape of the trailing wake sheet S_W is prescribed using semi-empirical models. For the problem of cavitating flow, the approach presented by Fine (1992) is used. Here, since the cavitating portions S_{CB} and S_{CW} are unknown, an iterative solution procedure is required.

More details on the implementation of the sheet cavitation model can be found in Regener (2016). More detailed information on the underlying theory can be found in the book of Katz and Plotkin (2001).

References

Ainslie, M.A., Halvorsen, M.B., Robinson, S.P., 2021. A terminology standard for underwater acoustics and the benefits of international standardization. IEEE J. Ocean. Eng. 47 (1), 179–200.

Arndt, R.E.A., 1995. Vortex cavitation. In: Green, S.I. (Ed.), Fluid Vortices. Springer Netherlands, Dordrecht, pp. 731–782. http://dx.doi.org/10.1007/978-94-011-0249-0_17.

Arndt, R., Pennings, P., Bosschers, J., van Terwisga, T., 2015. The singing vortex. Interface Focus 5 (5), 20150025. http://dx.doi.org/10.1098/rsfs.2015.0025.

Arveson, P.T., Vendittis, D.J., 2000. Radiated noise characteristics of a modern cargo ship. J. Acoust. Soc. Am. 107 (1), 118–129.

Berger, S., 2018. Numerical Analysis of Propeller-Induced Higher-Order Pressure Fluctuations on the Ship Hull (Ph.D. thesis). Hamburg University of Technology, Hamburg, http://dx.doi.org/10.15480/882.1605.

Bosschers, J., 2008. Analysis of inertial waves on inviscid cavitating vortices in relation to low-frequency radiated noise. In: WIMRC Cavitation Forum. Warwick University UK.

Bosschers, J., 2018a. Propeller Tip-Vortex Cavitation and Its Broadband Noise (Ph.D. thesis). University of Twente, http://dx.doi.org/10.3990/1.9789492679529.

Bosschers, J., 2018b. A semi-empirical prediction method for broadband hull-pressure fluctuations and underwater radiated noise by propeller tip vortex cavitation. J. Mar. Sci. Eng. 6 (2), http://dx.doi.org/10.3390/jmse6020049, URL: https://www.mdpi.com/2077-1312/6/2/49.

Brentner, K.S., Farassat, F., 2003. Modeling aerodynamically generated sound of helicopter rotors. Prog. Aerosp. Sci. 39 (2–3), 83–120. http://dx.doi.org/10.1016/s0376-0421(02)00068-4.

Bronshtein, I., Semendyayev, K., Musiol, G., Mühlig, H., 2015. Handbook of Mathematics. Springer Berlin Heidelberg, http://dx.doi.org/10.1007/978-3-662-46221-8.

Brooker, A., Humphrey, V., 2016. Measurement of radiated underwater noise from a small research vessel in shallow water. Ocean Eng. 120, 182–189. http://dx.doi.org/10.1016/j.oceaneng.2015.09.048.

Byrd, P.F., Friedman, M.D., 1971. Handbook of Elliptic Integrals for Engineers and Scientists. Springer Berlin Heidelberg, http://dx.doi.org/10.1007/978-3-642-65138-0.

Carey, W.M., 2009. Lloyd's mirror-image interference effects. Acoust. Today 5 (2), 14–20.

Choi, J., Chahine, G.L., 2003. Non-spherical bubble behavior in vortex flow fields. Comput. Mech. 32 (4–6), 281–290. http://dx.doi.org/10.1007/s00466-003-0485-5.

de Jong, C., 2009. Characterization of ships as sources of underwater noise. In: NAG/DAGA 2009 - Rotterdam.

De Robertis, A., Handegard, N.O., 2012. Fish avoidance of research vessels and the efficacy of noise-reduced vessels: a review. ICES J. Mar. Sci. 70 (1), 34–45. http://dx.doi.org/10.1093/icesjms/fss155.

European Commission, 2013. SONIC - suppression of underwater noise induced by cavitation. URL: http://www.sonic-fp7.eu/.

Farassat, F., 2007. Derivation of Formulations 1 and 1A of Farassat. Tech. Rep. TM-2007-214853, NASA.

Farassat, F., Brentner, K.S., 1998. The acoustic analogy and the prediction of the noise of rotating blades. Theor. Comput. Fluid Dyn. 10, 155–170. http://dx.doi.org/10.1007/s001620050056.

Farassat, F., Succi, G., 1982. The prediction of helicopter rotor discrete frequency noise. In: American Helicopter Society. pp. 497–507.

Ffowcs-Williams, J.E., Hawkings, D.L., 1969. Sound generation by turbulence and surfaces in arbitrary motion. Phil. Trans. R. Soc. A 264, 321–342. http://dx.doi.org/10.1098/rsta.1969.0031.

Ffowcs-Williams, J.E., Lighthill, J., 1971. Film notes for aerodynamic generation of sound. Presented at Imperial College of Science and Technology.

Ffowcs-Williams, J.E., O'shea, S., 1970. Sound generation by hydrodynamic sources near a cavitated line vortex. J. Fluid Mech. 43 (4), 675–688. http://dx.doi.org/10.1017/S0022112070002665.

Fine, N., 1992. Nonlinear Analysis of Cavitating Propellers in Nonunioform Flow (Ph.D. thesis). Massachusetts Institute of Technology, Cambridge.

Franc, J.-P., Michel, J.-M., 2005. The dynamics of spherical bubbles. In: Fundamentals of Cavitation. Springer, pp. 35–56.

Gosda, R., Perić, R., Abdel-Maksoud, M., 2021. Simulation of linear and non-linear dynamics of tip-vortex cavities with a panel method using explicit relaxation zones. In: 11th International Symposium on Cavitation. CAV2021.

Göttsche, U., 2020. Entwicklung einer numerischen Methode zur Vorhersage der hydroakustischen Schallabstrahlung von Schiffspropellern (Ph.D. thesis). Hamburg University of Technology, Hamburg, http://dx.doi.org/10.15480/882.2953.

Higuchi, H., Arndt, R.E.A., Rogers, M.F., 1989-12. Characteristics of tip vortex cavitation noise. J. Fluids Eng. 111 (4), 495–501. http://dx.doi.org/10.1115/1.3243674.

Humphrey, V., Brooker, A., Dambra, R., Firenze, E., 2015. Variability of underwater radiated ship noise measured using two hydrophone arrays. In: OCEANS 2015 - Genova. pp. 1–10. http://dx.doi.org/10.1109/OCEANS-Genova.2015.7271383.

ISO17208-1, 2016. Underwater Acoustics - Quantities and Procedures for Description and Measurement of Underwater Sound from Ships - Part 1: Requriements for Precision Measurements in Deep Water Used for Comparison Purposes. Standard, International Organization for Standardization, Geneva, CH.

ISO17208-2, 2019. Underwater Acoustics - Quantities and Procedures for Description and Measurement of Underwater Sound from Ships - Part 2: Determination of Source Levels from Deep Water Measurements. Standard, International Organization for Standardization, Geneva, CH.

ITTC, 2017. The Specialist Committee on Hydrodynamic Noise - Final Report and Recommendations to the 28th ITTC. Tech. Rep., International Towing Tank Conference.

Kanemaru, T., Ando, J., 2015. Numerical analysis of tip vortex cavitation on marine propeller using a simple surface panel method SQCM. In: Fourth International Symposium on Marine Propulsors. Austin, Texas.

Katz, J., Plotkin, A., 2001. Low-Speed Aerodynamics. Cambridge University Press, Cambridge.

Lighthill, M.J., 1952. On sound generated aerodynamically I. General theory. Proc. R. Soc. A 211 (1107), 564–587. http://dx.doi.org/10.1098/rspa.1952.0060.

Ligneul, P., 1988. Theory of tip vortex cavitation noise of a screw propeller operating in a wake. In: Symposium on Naval Hydrodynamics, 17th.

MacGillivray, A.O., Martin, S.B., Ainslie, M.A., Dolman, J.N., Li, Z., Warner, G.A., 2023. Measuring vessel underwater radiated noise in shallow water. J. Acoust. Soc. Am. 153 (3), 1506–1524.

Maines, B., Arndt, R.E.A., 1997. The case of the singing vortex. J. Fluids Eng. 119 (2), 271–276. http://dx.doi.org/10.1115/1.2819130.

Merziger, G., Mühlbach, G., Wille, D., Wirth, T., 2010. Formeln+ Hilfen zur höheren Mathematik. Binomi.

Mirsadraee, Y., 2019. Development of a Model for Propeller Tip Vortex Cavitation and Analysis of the Radiated Pressure Fluctuations (Ph.D. thesis). Technical University of Denmark, Kongens Lyngby, Denmark.

Mitson, R.B., Knudsen, H.P., 2003. Causes and effects of underwater noise on fish abundance estimation. Aquat. Living Resour. 16 (3), 255–263. http://dx.doi.org/10.1016/S0990-7440(03)00021-4.

Moore, S., 2019. Acoustic signature control on maritime platforms. In: Proceedings of ACOUSTICS, Vol. 10, No. 13.

Morozov, V., 1974. Theoretical analysis of acoustic-emission from cavitation line vortices. Sov. Phys. - Acoust.-USSR 19 (5), 468–471.

Regener, P., 2016. Hull-Propeller Interaction and Its Effect on Propeller Cavitation (Ph.D. thesis). Technical University of Denmark, Kongens Lyngby, Denmark, http://dx.doi.org/10.11581/DTU:00000032.

Ross, D., 1976. Mechanics of Underwater Noise. Pergamon Press.

Scharf, M., Göttsche, U., Beckmann, R., Bévand, R., Abdel-Maksoud, M., 2024. Prediction of the hydroacoustic emissions of a twin-screw vessel considering the phase angle of the propellers. In: 8th International Symposium on Marine Propulsors, Smp 2024. Berlin, pp. 701–708.

Seybert, A.F., Soenarko, B., Rizzo, F.J., Shippy, D.J., 1986. A special integral equation formulation for acoustic radiation and scattering for axisymmetric bodies and boundary conditions. J. Acoust. Soc. Am. 80 (4), 1241–1247. http://dx.doi.org/10.1121/1.393817.

Sezen, S., Atlar, M., 2022. Numerical investigation into the effects of tip vortex cavitation on propeller underwater radiated noise (URN) using a hybrid CFD method. Ocean Eng. 266, 112658. http://dx.doi.org/10.1016/j.oceaneng.2022.112658.

Szantyr, J., 2006. A computational model of propeller cavitating tip vortex interacting with the rudder. In: 6th International Symposium on Cavitation CAV2006. Wageningen, Netherlands.

Tani, G., Aktas, B., Viviani, M., Yilmaz, N., Miglianti, F., Ferrando, M., Atlar, M., 2019. Cavitation tunnel tests for "The Princess Royal" model propeller behind a 2-dimensional wake screen. Ocean Eng. 172, 829–843. http://dx.doi.org/10.1016/j.oceaneng.2018.11.017.

Testa, C., 2008. Acoustic Formulations for Aeronautical and Naval Rotorcraft Noise Prediction Based on the Ffowcs-Williams and Hawkings Equation (Ph.D. thesis). Università degli studi Roma Tre, Rome, URL: http://hdl.handle.net/2307/192.

Thomson, W., 1880. XXIV. Vibrations of a columnar vortex. Lond. Edinb. Dublin Philos. Mag. J. Sci. 10 (61), 155–168. http://dx.doi.org/10.1080/14786448008626912.

Turkmen, S., Aktas, B., Atlar, M., Sasaki, N., Sampson, R., Shi, W., 2017a. On-board measurement techniques to quantify underwater radiated noise level. Ocean Eng. 130, 166–175.

Turkmen, S., Atlar, M., Sasaki, N., 2017b. Full-scale measurements of underwater radiated noise of a catamaran research vessel. In: Fifth International Symposium on Marine Propulsors. Espoo, Finland.

Urban, H.G., 2002. Handbuch der Wasserschallteknik. STN ATLAS Elekronik GmbH, Bremen.

van Wijngaarden, E., Bosschers, J., Kuiper, G., 2005. Aspects of the cavitating propeller tip vortex as a source of inboard noise and vibration. In: Fluids Engineering Division Summer Meeting, Vol. 41995. pp. 539–544.

Yilmaz, N., Dong, X., Aktas, B., Yang, C., Atlar, M., Fitzsimmons, P.A., 2020. Experimental and numerical investigations of tip vortex cavitation for the propeller of a research vessel,"The Princess Royal". Ocean Eng. 215, 107881.